The Astrophysical Journal Letters, 887:L25 (20pp), 2019 December 10 https://doi.org/10.3847/2041-8213/ab53eb
© 2019. The American Astronomical Society. All rights reserved.

Constraining the Neutron Star Mass–Radius Relation and Dense Matter Equation of State with *NICER*. I. The Millisecond Pulsar X-Ray Data Set

Slavko Bogdanov[1], Sebastien Guillot[2,3], Paul S. Ray[4], Michael T. Wolff[4], Deepto Chakrabarty[5], Wynn C. G. Ho[6,7], Matthew Kerr[4], Frederick K. Lamb[8,9], Andrea Lommen[6], Renee M. Ludlam[10,22], Reilly Milburn[6], Sergio Montano[6], M. Coleman Miller[11], Michi Bauböck[12], Feryal Özel[13], Dimitrios Psaltis[13], Ronald A. Remillard[5], Thomas E. Riley[14], James F. Steiner[15], Tod E. Strohmayer[16], Anna L. Watts[14], Kent S. Wood[17], Jesse Zeldes[6], Teruaki Enoto[18], Takashi Okajima[19], James W. Kellogg[20], Charles Baker[20], Craig B. Markwardt[21], Zaven Arzoumanian[21], and Keith C. Gendreau[21]

[1] Columbia Astrophysics Laboratory, Columbia University, 550 West 120th Street, New York, NY 10027, USA; slavko@astro.columbia.edu
[2] IRAP, CNRS, 9 avenue du Colonel Roche, BP 44346, F-31028 Toulouse Cedex 4, France
[3] Université de Toulouse, CNES, UPS-OMP, F-31028 Toulouse, France
[4] Space Science Division, U.S. Naval Research Laboratory, Washington, DC 20375, USA
[5] MIT Kavli Institute for Astrophysics and Space Research, Massachusetts Institute of Technology, 70 Vassar Street, Cambridge, MA 02139, USA
[6] Department of Physics and Astronomy, Haverford College, 370 Lancaster Avenue, Haverford, PA 19041, USA
[7] Mathematical Sciences, Physics and Astronomy, and STAG Research Centre, University of Southampton, Southampton SO17 1BJ, UK
[8] Center for Theoretical Astrophysics and Department of Physics, University of Illinois at Urbana-Champaign, 1110 West Green Street, Urbana, IL 61801-3080, USA
[9] Department of Astronomy, University of Illinois at Urbana-Champaign, 1002 West Green Street, Urbana, IL 61801-3074, USA
[10] Cahill Center for Astronomy and Astrophysics, California Institute of Technology, Pasadena, CA 91125, USA
[11] Department of Astronomy and Joint Space-Science Institute, University of Maryland, College Park, MD 20742-2421, USA
[12] Max Planck Institut für Extraterrestrische Physik, Gießenbachstr. 1, D-85737 Garching, Germany
[13] Steward Observatory, University of Arizona, 933 N. Cherry Avenue, Tucson, AZ 85721, USA
[14] Anton Pannekoek Institute for Astronomy, University of Amsterdam, Science Park 904, 1090GE Amsterdam, The Netherlands
[15] Harvard-Smithsonian Center for Astrophysics, 60 Garden Street, Cambridge, MA 02138, USA
[16] Astrophysics Science Division and Joint Space-Science Institute, NASA Goddard Space Flight Center, Greenbelt, MD 20771, USA
[17] Praxis, resident at the U.S. Naval Research Laboratory, Washington, DC 20375, USA
[18] The Hakubi Center for Advanced Research and Department of Astronomy, Kyoto University, Kyoto 606-8302, Japan
[19] Astrophysics Science Division, NASA Goddard Space Flight Center, Greenbelt, MD 20771, USA
[20] Applied Engineering and Technology Directorate, NASA Goddard Space Flight Center, Greenbelt, MD 20771, USA
[21] X-Ray Astrophysics Laboratory, NASA Goddard Space Flight Center, Greenbelt, MD 20771, USA
Received 2019 September 5; revised 2019 October 16; accepted 2019 October 18; published 2019 December 12

Abstract

We present the set of deep *Neutron Star Interior Composition Explorer* (*NICER*) X-ray timing observations of the nearby rotation-powered millisecond pulsars PSRs J0437−4715, J0030+0451, J1231−1411, and J2124−3358, selected as targets for constraining the mass–radius relation of neutron stars and the dense matter equation of state (EoS) via modeling of their pulsed thermal X-ray emission. We describe the instrument, observations, and data processing/reduction procedures, as well as the series of investigations conducted to ensure that the properties of the data sets are suitable for parameter estimation analyses to produce reliable constraints on the neutron star mass–radius relation and the dense matter EoS. We find that the long-term timing and flux behavior and the Fourier-domain properties of the event data do not exhibit any anomalies that could adversely affect the intended measurements. From phase-selected spectroscopy, we find that emission from the individual pulse peaks is well described by a single-temperature hydrogen atmosphere spectrum, with the exception of PSR J0437−4715, for which multiple temperatures are required.

Unified Astronomy Thesaurus concepts: Neutron stars (1108); Pulsars (1306); Compact objects (288); Nuclear astrophysics (1129); Millisecond pulsars (1062); X-ray astronomy (1810); X-ray observatories (1819); Pulsar timing method (1305); Spectroscopy (1558); Astronomical techniques (1684)

1. Introduction

Neutron stars (NSs) provide the only known setting where the regime of ultra-high density, large proton/neutron number asymmetry, and low temperature can be explored. NSs are therefore of tremendous value for nuclear physics, as they offer a path to empirically determining the state of cold, catalyzed matter beyond nuclear saturation density ($\rho_s = 2.8 \times 10^{14}$ g cm^{-3}). Determining the dense matter equation of state (EoS) has far-reaching implications for astrophysics as well. The detailed physics and the accompanying electromagnetic, neutrino, and gravitational wave signals of energetic astrophysical phenomena such as black hole/NS and double NS mergers, and core-collapse supernovae, are highly sensitive to the interior structure of NSs (Shibata & Taniguchi 2011; Faber & Rasio 2012; Del Pozzo et al. 2013; Read et al. 2013; Lackey et al. 2014; Kumar & Zhang 2015; Rosswog 2015; Bauswein et al. 2016; Fernández & Metzger 2016; Janka et al. 2016; Oertel et al. 2017; Shibata 2016).

Because we cannot directly sample the matter at the core of an NS, we must rely on indirect inference using sensitive observations of their exteriors. Fortunately, the microscopic relation between the pressure P and density ρ of NS matter determines the macroscopic properties of the star, in particular, its radius R and mass M (see, e.g., Lattimer & Prakash 2001, 2005; Özel & Psaltis 2009; Read et al. 2009;

[22] NASA Einstein Fellow.

Hebeler et al. 2013; Özel & Freire 2016). This connection between the two relations can, in principle, be exploited via astrophysical observations to derive tight constraints on these parameters in any given parameterization of the EoS (see, e.g., Greif et al. 2019; Miller et al. 2019a, and references therein).

This prospect has prompted a number of efforts using a variety of methods to constrain the mass–radius (M–R) relation of NSs with X-ray observations, complementary to those that aim to constrain R and the dense matter EoS using detections of gravitational waves from binary NS mergers with the Advanced Laser Interferometer Gravitational-Wave Observatory (LIGO) and VIRGO gravitational wave observatories (Abbott et al. 2018). In practice, constraining the M–R relation with X-ray observations has proven to be quite difficult due to the absence of strong spectral lines, or ambiguity as to the nature of observed emission features (e.g., Cottam et al. 2002; Chang et al. 2006; Rauch et al. 2008; Lin et al. 2010). Thermal X-ray radiation from the physical surface of an NS can be used to extract valuable information regarding the EoS (e.g., Heinke 2013; Miller 2013; Özel 2013; Potekhin 2014; Özel & Freire 2016, for comprehensive reviews). Although most existing measurements yield values of R that are generally consistent with the expected range of theoretical values, even for nominally precise measurements there are enough concerns about systematic errors that it is not yet possible to constrain the EoS significantly (see, e.g., Steiner et al. 2010, 2018; Leahy et al. 2011; Guillot et al. 2013; Heinke et al. 2014; Miller & Lamb 2016; Özel et al. 2016; Nättilä et al. 2017).

For rapidly rotating NSs with the surface X-ray radiation contained in regions smaller than the whole stellar surface, R and M can be constrained individually through careful modeling of the observed X-ray pulsations. This is possible because the characteristics of the pulsations depend on R and M in different ways (Pechenick et al. 1983; Strohmayer 1992; Page 1995; Miller & Lamb 1998; Braje et al. 2000; Beloborodov 2002; Poutanen & Gierliński 2003; Cadeau et al. 2007; Morsink et al. 2007; Lo et al. 2013; Psaltis & Özel 2014; Psaltis et al. 2014; Miller & Lamb 2015).

The *Neutron Star Interior Composition Explorer* (*NICER*; see Gendreau et al. 2016), operating on the *International Space Station* (*ISS*) since 2017 June, is focusing on measuring R and M of a few nearby rotation-powered millisecond pulsars (MSPs) that produce thermal radiation by fitting model pulse profiles to these periodic soft X-ray modulations. These targets have been selected because their X-rays appear to be produced primarily by thermal emission from hotter regions around their magnetic poles. The pulsations are always present, the beaming pattern and spectrum of the emission that produces them is thought to be relatively well understood, and the rotation rates of these stars are rapid and exceptionally stable. Moreover, based on simulations, it is expected that (unlike the case for other methods) if a fit to the joint phase and energy properties of *NICER* MSP X-ray pulsations is statistically good, it is not strongly biased (see, e.g., Lo et al. 2013; Miller & Lamb 2015). Rotation-powered MSPs are, in this regard, more favorable for R and M measurements using *NICER* than are the modulations produced by (i) accretion-powered millisecond X-ray pulsars, which exhibit temporally varying pulsation properties with no widely accepted model of their X-ray emission, including nonthermal processes from poorly understood regions on and above the stellar surface (see, e.g., Hartman et al. 2008; Patruno & Watts 2012); or (ii) burst oscillation sources, which suffer, by comparison, from being extremely transient and from an uncertainty as to whether the hot spots always ignite in the same location (see, e.g., Watts 2012 for a review).

The present article is the first in a series of papers describing the data, model, and methodology for obtaining constraints on the NS M–R relation and the dense matter EoS. Here, we describe the targeted MSPs, their observations, and data sets obtained with *NICER*, the analyses of which will be published in subsequent works. In Bogdanov et al. (2019), Paper II, we present the approach and codes we use to describe the propagation of the photons emitted from the surface to the observer, while S. Bogdanov et al. (2019, in preparation), Paper III, describes all other aspects of the modeling technique applied to the *NICER* data and the potential sources of systematic error. The first set of results, for PSR J0030+0451, of the parameter estimation analyses that are based on the data described here to obtain estimates on M and R, as well as the dense matter EoS are presented in Miller et al. (2019b), Riley et al. (2019), and Raaijmakers et al. (2019). Results for the other targets will be presented in subsequent publications. The work is organized as follows: in Section 2, we describe the *NICER* telescope and its performance. In Section 3, we detail the observations and data reduction procedures used to obtain the MSP event lists used for parameter estimation analyses. Section 4 deals with non-source background emission specific to *NICER* and the methods used to estimate it. In Section 5 we provide a brief overview of the history of X-ray observations of rotation-powered MSPs. In Section 6, we discuss the four targeted MSPs and the corresponding *NICER* spin phase-folded data. Section 7 focuses on the event folding, long-term timing, and Fourier-domain properties of the event data. In Section 8, we present phase-selected spectroscopy of the four MSPs. We offer conclusions in Section 9.

2. The *NICER* X-ray Timing Instrument (XTI) Instrument Performance and Calibration

The *NICER* XTI consists of an array of 52 active silicon drift detectors housed in focal plane modules (FPMs), each paired with a nested single-reflection grazing-incidence "concentrator" optic assembly in the optical path. Groups of eight FPMs are controlled by a single Measurement and Power Unit (MPU). The XTI's concentrator optics are co-aligned, collecting sky emission from a single $\approx 3'$ radius non-imaging field of view (FOV). The instrument is sensitive to X-rays in the 0.2–12 keV band, with a peak effective area of $\approx$1900 cm^2 around 1.5 keV (Gendreau et al. 2016). The lower bound is dictated by absorption in optical-blocking filters, electronic noise in the cooled detectors, and increasing optical light-loading noise at the lowest energies, while the upper bound is driven by a decline in grazing-incidence reflectivity as well as the quantum efficiency of the silicon detectors.

Photons or charged particles incident on the XTI silicon drift detectors induce an amplified charge signal, which is processed in parallel by a slow and fast analog chain with 465 ns and 85 ns shaping time constants, respectively (Prigozhin et al. 2016). The slow chain provides a more precise energy measurement, while the fast chain provides a more precise arrival time measurement of the incident event. Signals that are above a preset threshold in each chain produce an electronic trigger that causes the arrival time and pulse height amplitude of the incident event to be sampled and digitized. Events that cause both chains to trigger have their fast chain timestamp

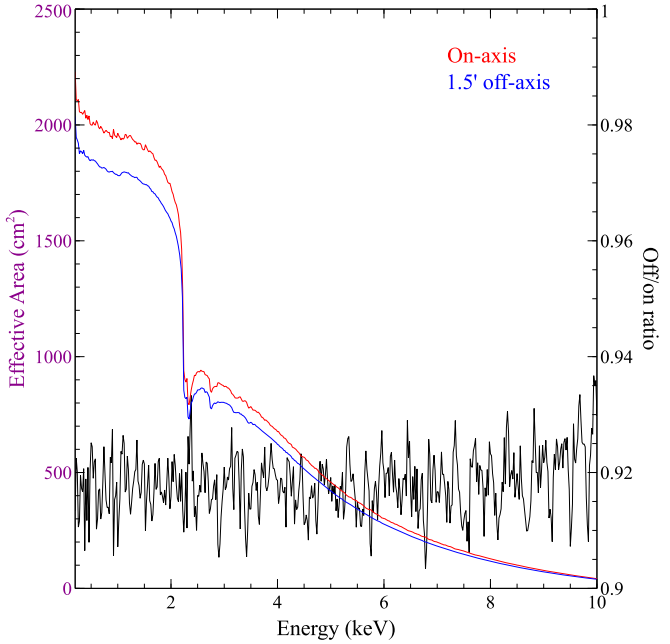

Figure 1. Effective area (red line) of the *NICER* XTI concentrator optics as a function of photon energy, derived from ray-tracing simulations and neglecting low-energy absorption from filters in the optical path; also shown is the estimated effective area (blue line) at 1.′5 off axis, appropriate for the *NICER* observations of PSR J0437−4715 (see the Appendix for details). The reduction in sensitivity of the off-axis response has weak or no energy dependence, as shown by the ratio of the off- and on-axis spectrum ratio (black line) measured via observations of the Crab Nebula and pulsar; variations from channel to channel are due to statistical fluctuations.

reported; otherwise, the slow chain timestamp is reported. Whether the chain triggers depends on the event pulse height (which is approximately proportional to the energy deposition within the detector), such that events with energies $E \lesssim 1$ keV do not trigger the fast chain, while higher-energy events will trigger both chains. This includes X-rays as well as energetic particles and γ-rays produced by particle interactions with the detector or surrounding structure of *NICER*.

The fast chain timing uncertainty is 70 ns. The slow minus fast timing uncertainty is <4 ns, so that the two analog chains have nearly identical timing uncertainties. Time biases are typically ∼250 ns for the fast chain and ∼760 ns for the slow chain for individual *NICER* detectors, and timing variations between individual detectors are typically ∼11 ns. The measured biases are corrected using *NICER* standard software (`nicertimecal`). The *NICER*-calibrated event timestamp values after this calibration is performed refer to the time that an on-axis X-ray or particle entered the detector aperture. The timestamp of an event is referenced to the GPS receiver on *NICER*. For the intended analysis of the MSP pulse profiles, the time binning is the pulse period of a few ms divided by 32, compared to which any *NICER* time-tagging uncertainties are negligible.

For the analyses of the *NICER* data presented here, we used products from the calibration database (CALDB) version 20181105 and gain solution (the relationship between energy deposition and pulse height) version `optmv7`. The on-axis effective area including all 52 active detectors is shown in Figure 1. As described in the Appendix, for PSRs J0437−4715 and J2124−3358 we use offset pointings to minimize contamination from neighboring background sources. Because these pulsars are observed off axis, for their parameter estimation analyses it is necessary to consider an effective area curve that accounts for the resulting decline in sensitivity. For this purpose, we conducted observations of the Crab Nebula and pulsar both on axis and at an offset matching that used for the PSR J0437−4715 observations. On- and off-axis effective area curves derived from ray-tracing simulations, and the ratio between off- and on-axis Crab spectrum measurements, are shown in Figure 1.

Calibration of the effective area of the *NICER* XTI was carried out using observations of the Crab. The energy-dependent residuals in the fits to the Crab spectrum are typically at the level of $\lesssim$2%, likely stemming from a lack of knowledge of the detailed microphysics of the concentrator optics. Efforts are under way by the *NICER* calibration team to further improve the instrument model.

Table 1
NICER Observations of the Four Millisecond Pulsars Studied Here

Pulsar	ObsID Range	Raw Exposure (Ms)	Total Filtered Exposure (Ms)
PSR J0437–4715	0060010101–0060010110	0.071	0.951
	1060010101–1060010439	2.098	
	2060010401–2060010405	0.032	
PSR J0030+0451	1060020101–1060020437	3.076	1.936
PSR J1231–1411	0060060101–0060060113	0.108	1.356
	1060060101–1060060373	1.982	
	2060060301–1060060389	0.395	
PSR J2124–3358	0060040101–0060040104	0.003	1.051
	1060040101–1060040313	1.377	
	2060040301–1060040348	0.288	

Note. The exposure time columns report the total duration of data collection ("Raw"), and the exposure time after the filtering described in Section 3.

3. Observations and Data Reduction

The data sets considered here were acquired over the period starting in 2017 through 2019 June. Owing to the 92 minutes orbit of the *ISS*, events are typically accumulated in a large number of separate exposures, each lasting several hundred to ∼2000 s. Exposures obtained during the same UTC days are grouped into a single observation (ObsID). The observations for the four MSPs discussed here are summarized in Table 1. The data processing and filtering was performed using HEASoft 6.25[23] and NICERDAS version 5.0. For all sources, the initial event lists are subjected to the same standard filtering criteria:

1. *Maximum angular distance from target*. For standard *NICER* science analyses, event data for a particular target are considered valid if the XTI boresight is within 0.°015 of the source position. This same criterion is applied to the MSP data that we consider here.
2. *South Atlantic Anomaly passages and particle background excision*. Particle background is particularly severe during times when the *ISS* is near the South Atlantic Anomaly (SAA). Particle-induced events typically have very high amplitudes and/or occur far from

[23] https://heasarc.nasa.gov/lheasoft/

the center of the detector. Many of these events can be filtered out of the event list to produce a cleaned list of predominantly X-ray–only events using the detected amplitude and/or offset from the detector center. This is possible because the entrance aperture of each FPM for X-rays is only 2 mm in diameter, while the entire active area of the physical detector is 25 mm^2 (Prigozhin et al. 2016). The ratio of pulse invariant (PI) amplitudes for events detected in both the slow and fast chains, PI_RATIO = PI_SLOW/PI_FAST, is related to the event offset from the center of the detector. Events with PI_RATIO $> 1.1 + 120/PI$ are likely particle events and are normally excluded from standard X-ray analysis. This is called "trumpet" filtering because the PI versus PI_RATIO cloud resembles a trumpet.[24]

3. *Minimum elevation above Earth limb and bright Earth limb*. Observations with a pointing direction close to the limb of the Earth can be strongly affected by optical light-loading noise, especially during orbit day (bright Earth). Therefore, events are filtered to only include intervals when the elevation of the pointing direction above the Earth's limb is $>20°$ and $>30°$ above the bright Earth (ELV $> 20°$ and BR_EARTH $> 30°$).
4. *Exclusion of times of bad tracking*. *NICER* event data for a particular source are included only if the telescope is on target. The required conditions for good source tracking are determined using parameters provided in the auxiliary "make filter" (MKF) file, specifically ATT_MODE = 1, ATT_SUBMODE_AZ = 2, ATT_SUBMODE_EL = 2. In addition, times when the star tracker solution is not valid are filtered out, when the condition ST_VALID = 1 is not met.

The data sets were further screened using additional event filtering criteria, tailored for the purposes of pulse profile modeling. These include the following:

1. *Minimum number of enabled detectors*—For a variety of reasons, not all FPMs are actively registering events at all times. In the standard *NICER* data processing, the default filtering removes all good time intervals (GTIs) with fewer than 38 active detectors (defined through the MIN_FPM parameter). However, to ensure uniformity of the MSP data sets such that the effective area over time is constant (thus only requiring a single, time-average effective area curve in our analyses), we imposed a stricter requirement of accepting only GTIs during which all 52 FPMs are active.

For the intended analysis of these data, we are interested in the thermal X-rays that originate from the surface of the observed NSs. However, a significant subset of the events collected for each target have different origins and contribute to a background emission component. Both particles and local (non-cosmic) high-energy photons can generate events detected by the FPMs. There are a number of sources of local electromagnetic background radiation that can affect *NICER* X-ray data. Some of this background is removed by the standard processing pipeline, but residual background events may remain in the cleaned data. For instance, because *NICER* XTI is a non-imaging instrument, a portion of the emission comes from the unresolved diffuse X-ray background as well as other point sources that fall within the $\sim 6'$ diameter telescope FOV; see Figures 7 and 8. In the Appendix we examine this contribution to the background for each MSP, in order to determine the optimal pointing that provides the best signal-to-noise ratio (S/N). Solar wind charge exchange also contributes to the background and occurs when a high charge state ion in the solar wind exchanges charge with a neutral species; the resultant ion is in an excited state and in the transition to the ground state can emit a soft X-ray photon.

There are other sources of background emission that are specific to *NICER* and which motivated additional filtering:

1. *Exclusion of "hot" detectors*. Three of the active FPMs (DET_ID 14, 34, and 54) are often found to exhibit count rates well above the average of the other detectors, with DET_ID 34 exhibiting such behavior most frequently. For this reason, from the GTIs with 52 active FPMs we removed events from these "hot" detectors. Removing only events from detector 34 produces similar clean exposure times and count rates compared to removing all three. In Miller et al. (2019b), the *NICER* data for PSR J0030+0451 were cleaned by removing DET_ID 34, while in Riley et al. (2019), the data with DET_ID 14, 34, and 52 removed were analyzed. The effective area was reduced by the appropriate amount (51/52 or 49/52) to account for the use of fewer detectors.
2. *Sun angle limits*. Sunlight produces detected noise events at low offset angles from the Sun, and potentially also for low bright Earth offset angles. In addition, sunlight reflecting off of the *ISS* solar panels or other *ISS* structures can be reflected into a subset of *NICER* FPMs. Solar radiation, whether direct or reflected, usually affects the low-energy ($E \ll 1$ keV) portion of the spectrum. The result is a light-loading noise peak at very low ($E < 0.3$ keV) energies. This noise peak exhibits a Gaussian-like energy distribution with a variable amplitude. When the amplitude is large, the tail of the Gaussian distribution may leak into higher energies, up to $\sim 0.4-0.5$ keV. This is common in certain, especially light-sensitive detectors, notably FPM 34. This additional low-energy background is not desirable as the MSP targets considered here have relatively soft spectra. Based on this, we filter the data such that we only include observations obtained at angles greater than $80°$ with respect to the Sun (SUN_ANGLE > 80).
3. *Variable background filtering*. The target MSPs considered here are expected to show no short- or long-term flux variability in their surface thermal emission. Therefore, any variability observed in the *NICER* data has a non-source origin and is usually due to local (non-cosmic) radiation and particle events. Even after standard filtering, short-lived instances (lasting seconds to minutes) of intense background flaring reaching count rates up to ~ 100 count s^{-1} are occasionally still present in the data. Such intervals are excised from the event lists by constructing a binned time series light curve with a 16 s resolution in the 0.25–8 keV band and applying a filter that removes all time bins that exceed a threshold count rate. The count rate cuts applied for PSRs J0437−4715, J0030+0451, J1231−1411, J2124−3358 are 3.5, 3.0, 3.0, and 2.8 count s^{-1}, respectively, which correspond approximately to a cutoff at $+2\sigma$ from the mean rate.

[24] See, e.g., Figure 6 at https://heasarc.gsfc.nasa.gov/docs/nicer/mission_guide/.

4. *Filtering by photon energy*. For all targets, we limit our analysis to events above 0.25 keV (corresponding to detector channel $\geqslant$25), because at lower energies there is increased noise from optical loading and there is greater uncertainty in the triggering efficiency for events. Because the MSPs under consideration have relatively soft spectra, for the parameter estimation analyses we also ignore all events above 3 keV (detector channel $\geqslant$300), where the thermal emission becomes negligible and the non-source background greatly dominates.

4. Background Modeling

As noted above, a portion of the non-source background contained in a typical *NICER* data set originates from the local environment of the telescope. The *NICER* team has developed two distinct approaches for modeling this time-dependent background emission.

The first method relies on a combination of two indicators of the space-weather environment, which are found to correlate closely with observed *NICER* background levels.

1. *The Cut0ff Rigidity*, as originally defined for the *BeppoSAX* mission (COR_SAX; see Campana et al. 2014 and references therein), is a measure of the minimum momentum per unit charge (expressed in units of GeV/c) a particle must have in order to reach a certain geographical location. Therefore, as defined, a lower COR_SAX value is an indication of higher background due to an increased influx of lower momentum particles.
2. *The planetary K-index* (K_p) is commonly used as a measure of geomagnetic storm activity and aurora strength; it quantifies disturbances in the horizontal component of Earth's magnetic field and is expressed as an integer in the range 0−9, with higher numbers indicating more activity (Lincoln 1967).

This "environmental" background model also uses the SUN_ANGLE parameter, which helps describe the low-energy background produced by optical loading. COR_SAX and SUN_ANGLE are contained in the MKF file (either the standard auxil/ni*.mkf file distributed with processed data or the augmented MKF file produced by the `niprefilter2` tool distributed with the NICERDAS HEASoft package). This background creation method uses two files: (i) the background events file[25] that serves as a reference library, and (ii) the KP. fits file.[26]

The diffuse cosmic X-ray background in the *NICER* blank fields (pointings of the *Rossi X-Ray Timing Explorer* background fields; Jahoda et al. 2006) is included in the estimated model background as an average of exposures of seven blank fields, with weighting of the averaging adjusted to match the K_p and COR_SAX of the target data. The contribution from point sources within the specific FOV near the target is not included, hence if the latter is important it must be treated case by case, by dealing with the relevant field sources. To produce a background estimate for a particular observation, the background reference library is used to find data from prior observations of blank fields with similar combinations of COR_SAX, K_p, and SUN_ANGLE values, and interpolating between the tabulated values. This modeling approach is predictive, in the sense that it does not rely on any of the event data of the source under consideration.

The second background measurement technique (referred to as the "3C50" model) uses the actual source event data to estimate in-band background by matching background library entries with observed event rates in (i) the 15–17 keV range, where the performance of the XTI is such that effectively no astrophysical signal is expected, (ii) a region in PI–PI_RATIO[27] space selected to capture the non-focused background, and (iii) the slow chain noise band (<0.2 keV). The matching is done on 120 s intervals, and then an exposure-weighted sum of library spectra is computed. This background method has been implemented in HEASoft through the `nibackgen3C50` command.

For the spectroscopic analyses in Section 8, we employ the space-weather-based background models. We note that in the detailed parameter estimation analyses for PSR J0030+0451 presented in Miller et al. (2019b) and Riley et al. (2019), no estimated background is explicitly taken into account; instead, non-hot-spot emission in each detector channel is treated as a free parameter and is assumed to have no dependence on spin phase. The space-weather-based background estimate is used as a lower bound on the total emission that does not originate from the hot regions on the NS surface.

5. Rotation-powered MSPs

Rotation-powered ("recycled") MSPs are a population of old NSs ($\sim 10^9$ yr), characterized by rapid rotation rates (a few hundred Hz), exceptional rotational stability, and low inferred dipole magnetic fields ($\sim 10^{8-9}$ G). These NSs are commonly believed to arise from slowly rotating pulsars in low-mass X-ray binaries (Alpar et al. 1982; Radhakrishnan & Srinivasan 1982), which acquire rapid spin rates via accretion of matter and angular momentum. At the end of their spin-up phase they are reactivated as rotation-powered (radio and γ-ray loud) pulsars, meaning that the observed radiation is generated at the expense of the rotational kinetic energy of the NS. Rotation-powered MSPs were identified as pulsed X-ray sources by Becker & Trümper (1993) in observations with *ROSAT*.

Over the past two decades, extensive studies with *Chandra* and *XMM-Newton* have shown that many of these NSs are detected as X-ray sources due to thermal emission with temperatures of $\sim 10^6$ K (Bogdanov et al. 2006, 2011; Zavlin 2006; Forestell et al. 2014). The inferred emitting areas indicate that this radiation is localized in regions on the stellar surface that are much smaller than the total surface area, but comparable to what is expected for pulsar magnetic polar caps. This finding is consistent with pulsar electrodynamics models, which predict heating of the polar caps by a backflow of energetic particles along the open magnetic field lines (Harding & Muslimov 2002; Lockhart et al. 2019). The potential utility of recycled MSPs as powerful probes of the NS structure was first pointed out by Pavlov & Zavlin (1997) and Zavlin & Pavlov (1998), who used *ROSAT* data of the nearest known MSP, PSR J0437–4715 (Johnston et al. 1993), to demonstrate that a model of polar cap thermal emission from an NS hydrogen atmosphere provides an adequate description of the

[25] Current version: https://heasarc.gsfc.nasa.gov/FTP/caldb/data/nicer/xti/pcf/30nov18targskc_enhanced.evt.

[26] The most current version, updated daily, is available at https://heasarc.gsfc.nasa.gov/FTP/caldb/data/gen/pcf/kp.fits.

[27] The PI_RATIO is defined as the ratio of the PI values measured by slow and fast chains, PI_RATIO = PI_SLOW/PI_FAST.

Table 2
MSPs Selected for *M–R* and EoS Constraints Using *NICER*

PSR	P (ms)	$\dot{P}$[a] ($\times 10^{-20}$)	D[b] (pc)	P_b (days)	$M_{\rm NS}$ ($M_\odot$)	M_c ($M_\odot$)	F_X[c] (erg cm^{-2} s^{-1})	*NICER* Rate[d] (ks^{-1})	References
J0437−4715	5.76	1.37	156.79(25)	5.741	1.44(7)	0.224(7)	1.29×10^{-12}	1430	(1), (2)
J0030+0451	4.87	1.02	325(9)	⋯	⋯	⋯	2.8×10^{-13}	314	(3), (4)
J1231−1411	3.68	0.76	420	1.860	unknown	$\geqslant$0.19	1.2×10^{-13}	210	(5)
J2124−3358	4.93	0.73	410^{+90}_{-70}	⋯	⋯	⋯	1.7×10^{-13}	110	(6), (7), (2)

Notes.
[a] Intrinsic spindown rates, corrected for proper motion.
[b] Distances with quoted uncertainties are based on parallax measurements. For PSR J1231−1411, the distance is estimated from its dispersion measure and the Yao et al. (2017) electron density model of the Galaxy.
[c] Unabsorbed source energy flux in the 0.25–2 keV band.
[d] *NICER* source count rate per ks in the 0.25–10 keV band.
References. (1) Johnston et al. (1993), (2) Reardon et al. (2016), (3) Lommen et al. (2000), (4) Arzoumanian et al. (2018), (5) Ransom et al. (2011), (6) Bailes et al. (1997), (7) Lynch et al. (2018).

X-ray pulse profiles of this MSP, as well as to place crude limits on the *M–R* relation.

Prompted by this promising result, deep *XMM-Newton* timing observations of nearby MSPs were conducted, which confirmed that a non-magnetic hydrogen atmosphere can reproduce the energy-dependent X-ray pulse profiles of the two closest known MSPs, PSRs J0437−4715 and J0030+0451. In contrast, the large-amplitude pulsations were found to be incompatible with a model that considers an isotropically emitting Planck spectrum. Furthermore, this modeling has already produced some constraints on the allowed NS *M–R* relation. For PSR J0437−4715, assuming 1.44 $M_\odot$ (the current best measurement from radio timing, including Shapiro delay measurements; Reardon et al. 2016) the stellar radius is constrained to be $R > 10.7$ km (at 3σ confidence; Bogdanov 2013), while for the isolated PSR J0030+0451 the best constraint is $R > 10.4$ km (at 99.9% confidence) assuming 1.4 $M_\odot$ (Bogdanov & Grindlay 2009). Although these existing limits are not particularly stringent they have nevertheless served to demonstrate the feasibility of this approach and have motivated the deep *NICER* observations described here.

6. The *NICER* MSP Target Sample

We now shift focus to the four brightest MSPs selected as primary targets for *M–R* constraints with *NICER*. For each pulsar we provide a brief overview of the relevant characteristics that make it an important *NICER* target and prior X-ray observations, and present the data obtained thus far. The spin parameters and binary properties (orbital period, NS mass, and companion mass, where applicable) of these pulsars are summarized in Table 2. In Guillot et al. (2019), we present *NICER* observations of other nearby rotation-powered MSPs conducted to assess their potential for providing additional *M–R* constraints in the future. In Z. Arzoumanian et al. (2019, in preparation), we present the *NICER* detection of thermal X-ray pulsations from PSRs J1614−2230 and J0740+6620, two of the three most massive NSs known ($M \approx 2\ M_\odot$). These targets will be the subject of parameter estimation analyses for *M–R* and dense matter EoS constraints in subsequent publications.

6.1. PSR J0437−4715

PSR J0437−4715 was discovered by Johnston et al. (1993) in the Parkes southern radio pulsar survey. At a distance of 156.79 ± 0.25 pc (Reardon et al. 2016), it is the nearest known MSP. It has properties typical of the Galactic population of MSPs, with a spin period $P = 5.76$ ms and intrinsic spindown rate (after kinematic corrections) of $\dot{P} \equiv dP/dt = 1.37 \times 10^{-20}$ s s^{-1}, implying a surface dipole magnetic field strength $B \approx 3 \times 10^8$ G, a characteristic age $\tau \approx 4.9$ Gyr, and spindown luminosity $\dot{E} \approx 3.8 \times 10^{33}$ erg s^{-1}. The pulsar is bound to a $M = 0.2\ M_\odot$ helium-core white dwarf companion in a 5.74 days circular orbit (Bailyn 1993).

PSR J0437−4715 is the first radio MSP to be detected as a pulsed X-ray source with the *ROSAT* Position Sensitive Proportional Counter (PSPC; Becker & Trümper 1993). Later, *XMM-Newton* observations in timing mode were used to place constraints on the NS radius with pulse profile modeling (see Bogdanov 2013). Spectrally, the ultraviolet (UV) to hard X-ray emission (∼0.01–20 keV) can be modeled with three thermal components and a nonthermal component (Durant et al. 2012; Bogdanov 2013; Guillot et al. 2016). The coldest thermal component describes the emission from the entire surface of the NS (excluding the hot spots), with a blackbody temperature $kT_{\rm BB} \sim 30$ eV. However, the size of the emission area is poorly constrained due to the limited sensitivity of X-ray instruments below ≈0.3 keV, and due to the limited coverage in the extreme UV regime where the Rayleigh–Jeans tail of this thermal component extends (Durant et al. 2012). The two hotter thermal components are interpreted as originating from the hot spots, and are best modeled with NS atmosphere spectral components (Bogdanov 2013). Finally, the nonthermal component is modeled with a simple power law, with a best-fit photon index $\Gamma = 1.50 \pm 0.25$, best constrained by *NuSTAR* observations in the hard X-ray band (Guillot et al. 2016). Timing analysis of these observations also revealed (3.7σ detection) pulsations at the NS spin period in the 2–20 keV band (Guillot et al. 2016). Above 6 keV, where the power-law component dominates over the thermal emission by more than 2 orders of magnitude, the detection significance of these pulsations drops to 2.4σ.

PSR J0437−4715 is located within $4\farcm18$ of a bright Seyfert II active galactic nucleus (AGN), RX J0437.4−4711 (Halpern & Marshall 1996). There are also 11 other sources within $6'$ of the pulsar, identified through archival imaging observations with *XMM-Newton*, and cataloged in the 3XMM-DR8 Catalog (Rosen et al. 2016). To minimize contamination due to the AGN and the other sources, we developed an optimization technique for the *NICER* pointing. This method, described in the Appendix, finds the optimal pointing that maximizes the S/N from the pulsar by minimizing the total flux from nearby

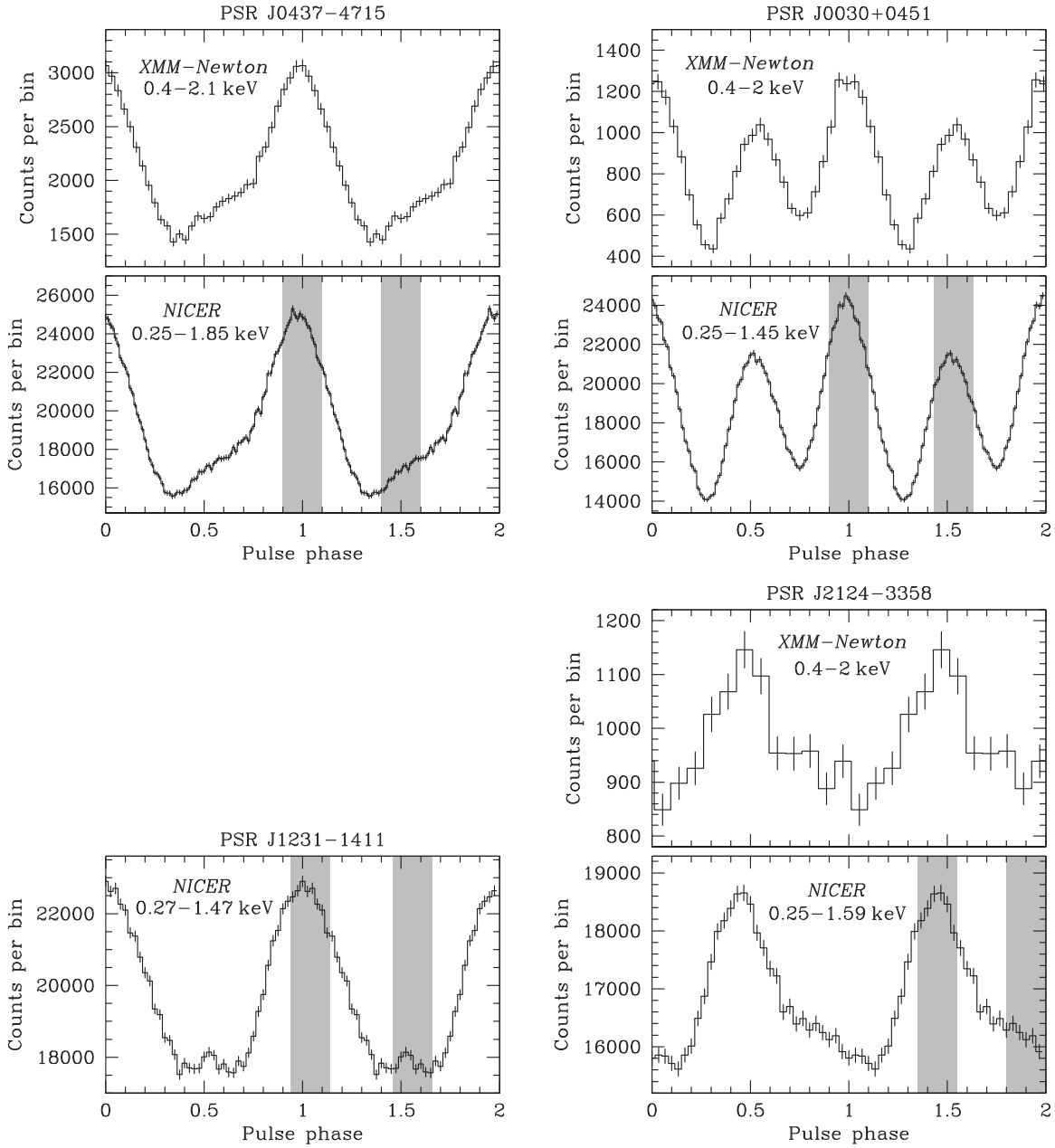

Figure 2. Folded profiles of PSR J0437–4715 (top left), PSR J0030+0451 (top right), PSR J1231−1411 (bottom left), and PSR J2124−3358 (bottom right). In all instances, phase zero is determined by the radio ephemeris used for event folding. The upper panel for each MSP shows the previous best X-ray profile obtained with *XMM-Newton* EPIC-pn, with the exception of PSR J1231−1411 for which no prior profile exists. The gray bands mark the phase intervals used for the phase-selected spectroscopy described in Section 8. Two rotational cycles are shown for clarity.

sources within the *NICER* FOV. For PSR J0437−4715, the optimal pointing position is 1.′5 to the southwest of the pulsar, where the pulsar S/N is 16% larger than for an on-source pointing. This is because, at the optimal pointing, the total contamination from other sources in the FOV amounts to 0.11 s^{-1}, while it would be 0.82 s^{-1} (dominated by the AGN) if the pulsar were placed at the center of the FOV.

PSR J0437−4715 has been observed regularly with *NICER* since the mission's commissioning phase, with exposures starting on 2017 July 6 (ObsID 0060010101). Here, we present data obtained through 2019 March 12 (ObsID 2060010405). The folded pulse profile from *NICER* based on 951 ks of clean exposure is shown in the upper-left panel of Figure 2. The strongest pulsed signal is found in the 0.25–1.85 keV range (at a 196.6σ single trial significance). The asymmetric pulse profile is now seen with greater clarity compared to previous observations, especially the "hump" around phases 0.5–0.7, which in Bogdanov (2013) is interpreted by invoking a second hot spot that is significantly displaced from the antipodal position relative to the primary spot. In the soft band (0.25–2 keV), where most of the source emission is found, the pulsations do not display any obvious changes as a function of energy (see the upper-left panel of Figure 3).

6.2. PSR J0030+0451

This solitary MSP was discovered at radio frequencies in the Arecibo drift scan survey (Lommen et al. 2000) and is one of the nearest known MSPs ($D = 325 \pm 9$ pc; Arzoumanian et al. 2018). Its spin period $P = 4.87$ ms and intrinsic spindown rate

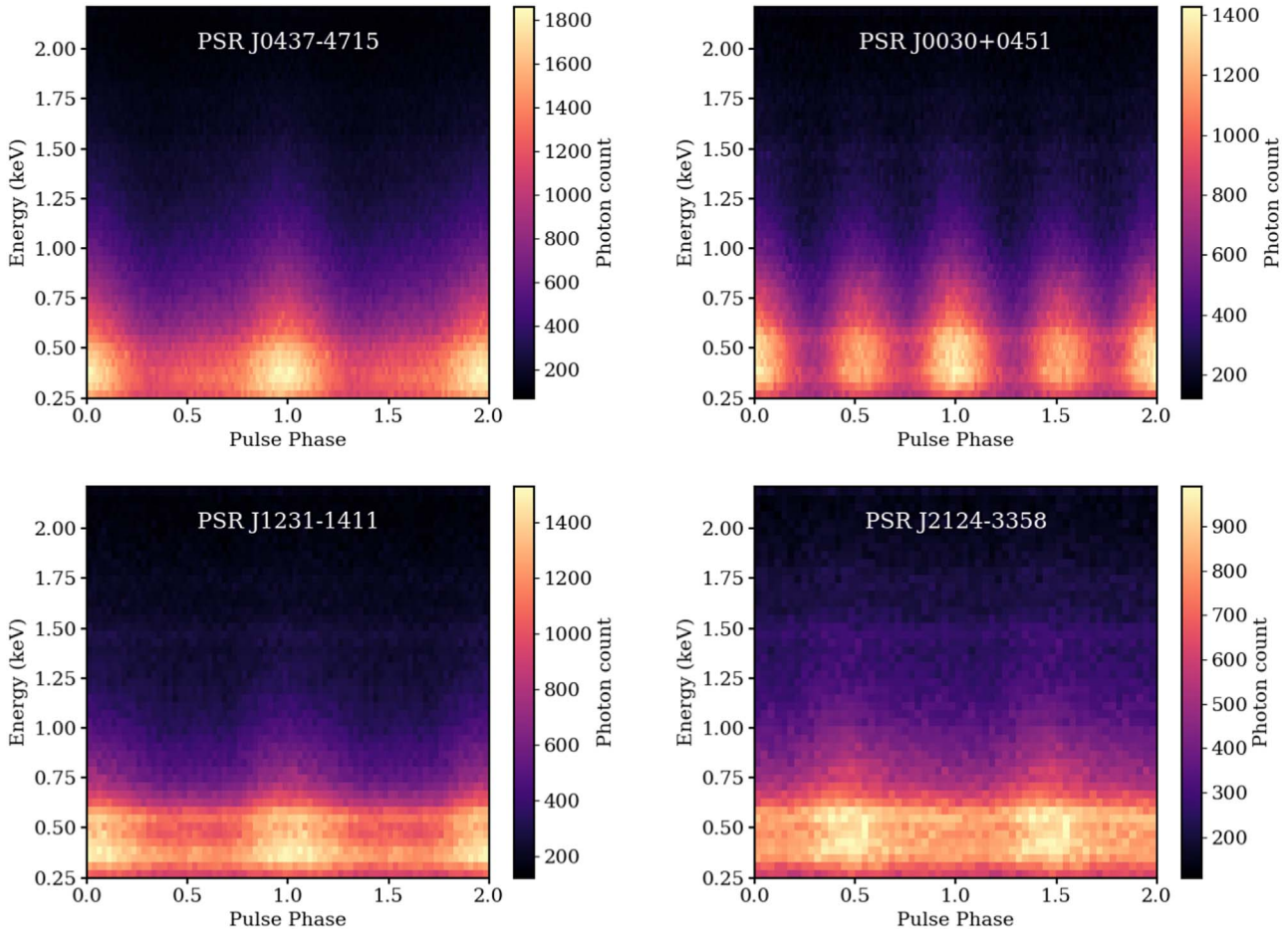

Figure 3. Two-dimensional histograms of *NICER* XTI counts vs. pulse phase and photon energy for PSRs J0437−4715, J0030+0451, J1231−1411, and J2124−3358. The color bar shows the number of counts in each pixel. Two pulse phase cycles are shown for clarity.

$\dot{P} = 1.02 \times 10^{-20}\,\mathrm{s\,s^{-1}}$ imply a surface dipole magnetic field strength $B \approx 2.7 \times 10^8$ G, a characteristic age $\tau \approx 7.8$ Gyr, and a spindown luminosity $\dot{E} \approx 3 \times 10^{33}\,\mathrm{erg\,s^{-1}}$. It was first detected in X-rays with *ROSAT* (Becker et al. 2000). Follow up observations with *XMM-Newton* (Becker & Aschenbach 2002; Bogdanov & Grindlay 2009) showed that its emission spectrum in the 0.1–10 keV energy range is remarkably similar to that of PSR J0437−4715, being well described by a predominantly thermal two-temperature model plus a faint hard tail evident above ∼3 keV. The pulsed emission in the 0.3–2 keV band is characterized by two broad pulses with pulsed fraction ∼60%–70%, which is consistent with a thermal origin of the X-rays, but only if the emission is significantly beamed such as may arise due to an atmosphere.

The environment around PSR J0030+0451 has many X-ray background sources. However, unlike the case of PSR J0437−4715, these sources do not strongly contaminate the source counts in the *NICER* observations. Our optimization method found that the pointing maximizing the S/N from the pulsar is 0.′25 in the northeast direction. However, the gain in S/N is ∼0.1%, and this small offset pointing can be safely neglected for PSR J0030+0451. Thus, for all observations of PSR J0030+0451, *NICER* was pointed at the pulsar position (see the Appendix).

The observations used for the parameter estimation analyses described in Miller et al. (2019b) and Riley et al. (2019) were acquired over the period between 2017 July 24 (ObsID 1060020101) and 2018 December 9 (ObsID 1060020412); the filtered and phase-folded event data set for PSR J0030+0451 is provided on Zenodo (doi:10.5281/zenodo.3524457). The *NICER* pulse profile based on the resulting 1.936 Ms of exposure in the 0.25–1.45 keV range (which yields the highest pulsed signal detection significance of 172.8σ) is shown in the upper-right panels of Figure 2. The high-quality data reveal that the double-peaked pulse profile retains its smoothness, as expected from surface thermal radiation from an NS, and confirm the significant difference in the amplitude of the two pulses and the depths of the two minima. In addition, as seen in Figure 3, the pulsed emission below ∼2 keV (where the source dominates above the background) remains unchanged in shape and phase alignment at all energies.

6.3. PSR J1231−1411

This $P = 3.68$ ms pulsar was discovered in a radio pulsar search campaign of unassociated *Fermi* Large Area Telescope (LAT) sources with the Green Bank Telescope (Ransom et al. 2011). PSR J1231−1411 is in a 1.86 days binary with a cool white dwarf companion. The pulsar dispersion measure implies a distance of 420 pc (Yao et al. 2017). *XMM-Newton* observations of this system have revealed a predominantly thermal spectrum (Ransom et al. 2011) reminiscent of PSRs J0437−4715 and J0030+0451. With a 0.2–12 keV flux of $1.9 \times 10^{-13}\,\mathrm{erg\,cm^{-2}\,s^{-1}}$, it is the third-brightest thermally emitting MSP and thus a well-suited target for *NICER*. Prior to

NICER there were no X-ray observations of this MSP with sufficiently high time resolution to enable the detection of its X-ray pulsations. Timing and phase-averaged spectroscopic analyses were carried out by Ray et al. (2019), based on a subset of the *NICER* data presented here.

The environment around PSR J1231−1411 has many X-ray background sources, but these sources are sufficiently faint to not contribute the majority of the expected counts during a *NICER* observation. As for other pulsars, we use the 3XMM-DR8 Catalog (Rosen et al. 2016) to characterize these nearby sources, infer their expected *NICER* count rates, and determine the optimal position to minimize their contribution to the background. For PSR J1231−1411, we adopted a strategy to point at the pulsar position, as the gain in S/N would be just ∼0.02% for an optimal offset pointing of 0.′27 (see the Appendix).

The data presented here are based on observations with *NICER* from 2017 June 26 to 2019 June 30, and include 440 ks of additional clean exposure compared to Ray et al. (2019), for a total of 1.36 Ms. The PSR J1231−1411 *NICER* profile in the 0.27–1.47 keV range (where the pulsed X-rays are detected at a maximum significance of 85σ) folded on the pulsar ephemeris from Ray et al. (2019) is shown in the lower-left panel of Figure 2. The pulse morphology is distinct from those of the other MSPs considered here, in that it features a prominent broad main pulse and a much weaker (but statistically highly significant) secondary pulse. This is indicative of a significantly different hot spot configuration and/or viewing angle. An interesting feature of the main pulse is its slight asymmetry, with a trailing edge that is broader than the leading edge. The pulsed emission from PSR J1231−1411 is significantly softer (see Figure 3 and Section 8) compared to PSRs J0437−4715 and J0030+0451, which is indicative of cooler polar caps.

6.4. PSR J2124−3358

PSR J2124−3358 is a nearby ($D = 410^{+90}_{-70}$ pc; Reardon et al. 2016), isolated MSP with a period $P = 4.93$ ms (Bailes et al. 1997). It was first detected in X-rays by the *ROSAT* High Resolution Imager (HRI; Becker & Trümper 1999). As the HRI provided no useful spectral information, only a total X-ray pulse profile was obtained, with pulsed fraction ∼33%. PSR J2124−3358 was observed with *Chandra* Advanced CCD Imaging Spectrometer S-array (ACIS-S) for 30.2 ks and with the *XMM-Newton* European Photon Imaging Camera (EPIC) for ∼70 ks (Hui & Becker 2006; Zavlin 2006). The spectrum of PSR J2124−3358 is also adequately described by predominantly thermal emission with a 0.25–2 keV unabsorbed flux of 1.7×10^{-13} erg cm^{-2} s^{-1}. This MSP is also surrounded by diffuse X-ray emission due to a pulsar wind nebula or bow shock (Hui & Becker 2006; Romani et al. 2017), contributing ∼4% to the total emission (therefore adding to the background). In addition, a handful of nearby sources within ∼6′ contribute to the observed *NICER* count rate. The optimal offset pointing that we chose is 1′ to the south of the pulsar, resulting in a gain in S/N of 1.7% compared to a pointing with the pulsar in the center of the FOV (see the Appendix).

The *NICER* observations of PSR J2124−3358 cover the period from 2017 June 26 through 2019 June 30. The *NICER* XTI pulse profile of PSR J2124−3358 in the 0.25–1.59 keV band (where it is detected at a single trial significance of 39.4σ) is shown in the lower-right panel of Figure 2. The substantial improvement in photon statistics compared to the previous *XMM-Newton* observation provide a much clearer sense of the pulse profile morphology. In particular, there is still no evidence for a distinct secondary pulse; instead, a trailing broad wing of the main pulse is now evident, resembling a mirrored version of the PSR J0437−4715 profile. Although the S/N of its pulse profile is lower compared to the other MSPs, PSR J2124−3358 also does not show any clear profile evolution as a function of energy below ∼2 keV.

7. Event Folding, Long-term Timing, and Flux Variability

7.1. Pulse Phase Assignment and Event Folding

To obtain the folded *NICER* pulse profiles using the entire span of available data, pulse phases were assigned to each event using two approaches.

1. Apply the barycentric correction using the `barycorr` tool in FTOOLS assuming the DE421 JPL solar system ephemeris (Folkner et al. 2009). Since the pulsars have measured proper motions, for each observation the position used for barycentering was computed based on the reference position and epoch and the measured proper motions in R.A. and decl. The resulting barycentered events were then folded with the pulsar ephemeris using the `tempo2` "photons" plug-in. We note that this procedure is not strictly correct because it does not account for the pulsar parallax. Nevertheless, given the relatively small apparent motions of the MSPs over the *NICER* data span, for the intended analysis this has a negligible effect ($\lesssim 1$ μs).
2. Using the `photonphase` tool from the PINT pulsar timing package[28] and the *NICER* orbit files (provided as one of the standard auxiliary products for each ObsID) to compute the transformation from the Terrestrial Time (TT) standard used for time tagging of *NICER* events to Barycentric Dynamical Time (TDB) and to assign pulse phases based on an input pulsar ephemeris. In this approach, the proper motion and parallax given in the timing solution are explicitly taken into account.

A comparison of the two methods shows differences at the level of $\lesssim 1$ μs in the form of a phase offset, which for the purposes of the analysis presented here is negligible. The results of the comparison of the two event folding approaches indicate that the procedures for assigning pulse phases to each event are reliable.

7.2. Long-term Timing

The energy-resolved pulse profiles used for the parameter estimation analyses aimed at constraining the neutron star *M–R* relation and the dense matter EoS are based on *NICER* observations carried out over time spans in the range 1.5–2 yr. This does not present an issue due to the extraordinary rotational stability of MSPs and the availability of precise long-term timing solutions obtained from radio observations, which, when combined with the exquisite absolute timing capabilities of *NICER*, permit the entire data set to be folded coherently at the pulsar period with negligible smearing of the pulse.

To verify this assertion, we grouped the *NICER* event data to produce time-of-arrival (TOA) measurements and compare them against the best available radio ephemerides. In particular,

[28] https://github.com/nanograv/pint

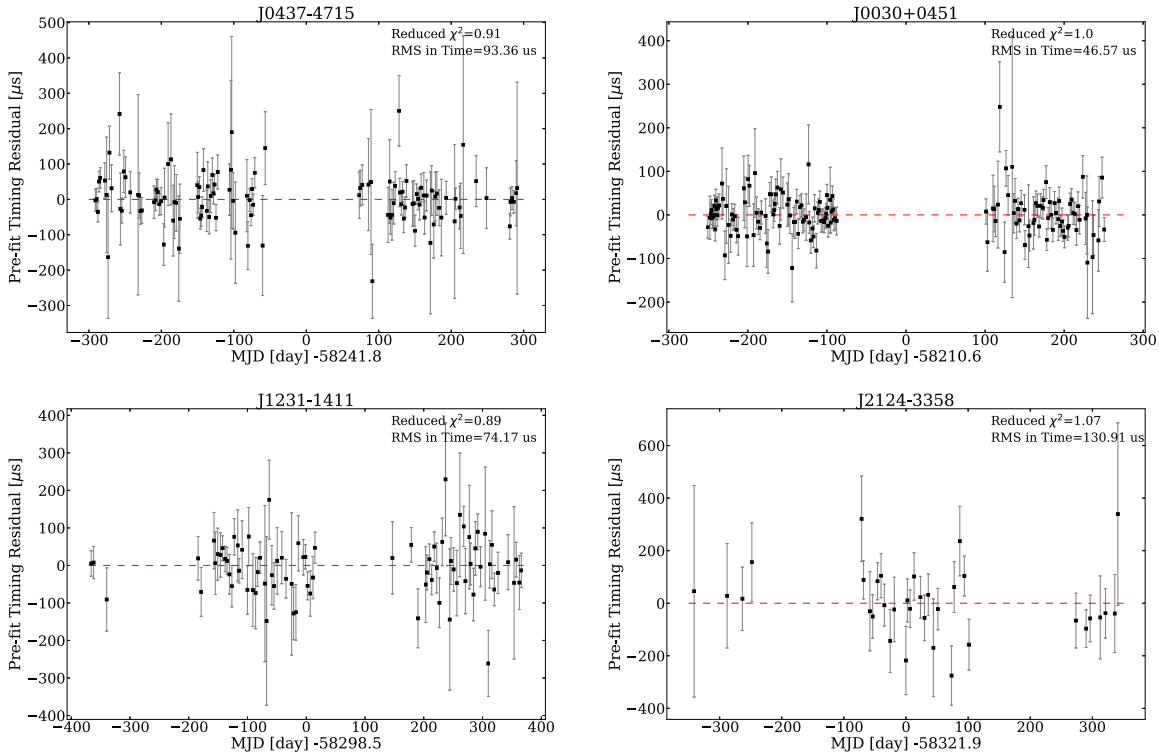

Figure 4. Timing residuals for PSR J0437−4715 (top left), PSR J0030+0451 (top right), PSR J1231−1411 (bottom left), and PSR J2124−3358 (bottom right) for *NICER* TOAs relative to the best available ephemeris for each pulsar.

for PSRs J0437−4715 and J2124−3358, we use the Parkes Pulsar Timing Array timing solutions from Reardon et al. (2016); for PSRs J0030+0451, we use the ephemeris from the NANOGrav 11 yr data set presented in Arzoumanian et al. (2018), and for PSR J1231−1411 we use the improved timing solution obtained by Ray et al. (2019) using *Fermi* LAT data. Each TOA was produced using 20 ks of effective observing time for PSRs J0437−4715 and J0030+0451 using the same filtering procedure described previously, while requiring that each TOA span a time less than two days (172.8 ks). An integration time of 50 ks per TOA was needed for PSRs J1231−1411 and J2124−3358 due to their dimmer nature and the maximum time span per TOA was relaxed to 4 days (345.6 ks) and 8 days (691.2 ks), respectively. The TOAs were measured by fitting the data to a double Gaussian template, then following the maximum likelihood model described in Ray et al. (2019). Fitting was performed using the `photon_toa` script from the NICERsoft package.[29] The residuals were produced using PINT, relative to the same radio timing solution used to create the profiles shown in Figures 2 and 3. Figure 4 shows the *NICER* timing residuals for PSRs J0437−4715, J0030+0451, J1231−1411, and J2124−3358 when compared against their respective radio ephemerides. We note that no fitting of the timing parameters was involved in this comparison; i.e., we kept all pulsar parameters fixed and only fitted for a global spin phase offset. It is evident that, in general, the *NICER* TOA measurements closely follow the radio timing solution as indicated by $\chi^2_\nu \approx 1$ in all cases. The resulting root-mean-square timing residuals are 44.01, 31.48, 53.07, and 100.13 μs for PSRs J0437−4715, J0030+0451, J1231−1411, and J2124−3358, respectively, which are at the expected level given the broad nature of the X-ray pulses. This provides assurance that folding the X-ray data over the entire observing span does not cause any smearing of the pulses that could negatively affect the desired *M–R* measurement by distorting the intrinsic shape of the profiles.

7.3. Long-term Flux Variability

The rotation-powered MSPs considered here were chosen as targets for *NICER* in part because they are not expected to exhibit any significant flux variability on timescales of years. Because the deep *NICER* data for each MSP span up to 2 yr, we can examine the long-term behavior of the thermal X-ray flux in further detail. One complication is that the background emission local to *NICER* (described in Section 4), including optical loading and energetic particles plus ambient (non-cosmic) radiation, exhibits long-term variability due to space weather, changing Sun angle, and the precession of the *ISS* orbit. Nevertheless, the pulsed component should be constant throughout, under the assumption that the polar cap radiation does not exhibit long-term temperature variations (caused, e.g., by variation in the return current).

To test for the presence of long-term variability, we divided each data set into a first half and a second half. The dividing point is determined by the halfway point in the counts, rather than the halfway point in time. For each half, we put the data into a form that has energy channels with 32 phase bins each. We use energy channels 25 through 299 (0.25–2.99 keV) inclusive, i.e., 275 energy channels ($\Delta E = 2.75$ keV). We compare the halves of the data in the following way. We arbitrarily designated one half the "data" and the other half the "model." If there is no change in the underlying pulsed emission then we expect the "model" to have the same fundamental folded profile as the "data," but the exposure time

[29] Available from https://github.com/paulray/NICERsoft.

might not be the same and the contributions from other sources (sky background, instrument noise, or space weather) could be different. The zero of phase might also be different. Thus our "model" has one parameter per energy channel (a phase-independent background[30]), one parameter for the ratio of exposure time between the "model" set and the "data" set, and one parameter for an overall shift in phase. We optimized the match between the model and data using these parameters. Using the optimized match, we then compute a χ^2 between the "model" and the "data" for each phase-channel bin $\chi^2(\mathrm{bin}) = (\mathrm{model} - \mathrm{data})^2/(\mathrm{model} + \mathrm{data})$, which is effectively like assuming that the variance of the model in each phase-channel bin is equal to the model in that bin, and similarly for the data, and that we can add the variances linearly to get the effective variance. Note that the sum of this pseudo-χ^2 value is not expected to follow a true χ^2 distribution exactly, because we are including the variance of the data from both halves. Nonetheless, this offers a rough indicator of whether the first and second halves are consistent with each other.

For PSRs J0437−4715, J0030+0451, J1231−1411, and J2124−3358, we find χ^2 values of 8433.32, 8841.09, 8457.03, and 8506.3, respectively, for 8523 degrees of freedom in all cases. The number of degrees of freedom is always $275 \times 32 - 275 - 2$, i.e., the number of phase-channel bins, minus the number of energy channels (because we have a free background parameter per channel) minus an overall exposure time factor minus a phase shift. For PSRs J0437−4715, J1231−1411, and J2124−3358 the χ^2 values are reassuringly small. For PSR J0030+0451, the formal probability of getting a χ^2 that large or larger with that many degrees of freedom, if the model is correct, is 0.8%. However, given that we do not expect exactly a χ^2 distribution, this is still consistent with no significant change between the first and second half for any of the four sources.

7.4. Fourier Decomposition of Pulse Profiles

One property of the pulsed thermal X-ray emission that is important for NS *M*–*R* constraints with the pulse profile modeling technique is the harmonic structure of the periodic signal. The anisotropic beaming pattern of NS atmospheres (e.g., Zavlin et al. 1996) causes the thermal pulsations to deviate from a sinusoidal shape, thus producing higher harmonics. Certain effects associated with the rapidly rotating NS such as occultation of the spot by the star, as well as Doppler boosting and aberration introduce extra harmonic content, thus providing useful information about *M* and *R*, which can be extracted through detailed modeling (Miller & Lamb 1998; Weinberg et al. 2001; Muno et al. 2002; Poutanen & Beloborodov 2006). As shown by Miller & Lamb (2015), for stars with spin rates less than ∼300 Hz, the presence of the first (and higher) overtones of the spin frequency in the pulsed emission is due primarily to (i) the non-isotropic beaming pattern of the radiation from the stellar surface and (ii) the self-occultation of the hot spot(s) by the star. The harmonic content of the data also provides information regarding the optimal phase binning of the data, so that no useful information is lost by binning too coarsely.

With this in mind, we have examined the detection significance of the harmonics in the *NICER* data as follows. Given a set of N photons with computed phases φ_i (in radians), we compute Fourier coefficients for harmonic k as

$$c_k = \frac{2}{N}\sum_i \cos k\varphi_i$$
$$s_k = \frac{2}{N}\sum_i \sin k\varphi_i. \quad (1)$$

The Fourier coefficients define an analytic model for the pulse profile. We can compare it to the data by binning the event data and computing the model for each bin, then constructing χ^2 as

$$\chi^2 = \sum_i \frac{(b_i - m_i)^2}{b_i} \quad (2)$$

where b_i is the binned data and m_i is the model prediction for that bin. If the fit is good, the residuals should be uncorrelated white noise (Poisson distributed, but effectively Gaussian-like for large numbers of counts per bin) and the reduced χ^2_ν (χ^2 per degree of freedom (d.o.f.)) should be close to unity. Figure 5 shows the results of the fits of the model profile constructed from the first four harmonically related sinusoids to the folded and binned profiles of PSRs J0437−4715, J0030+0451, J2124−3358, and J1231−1411. For all MSPs, we find that four harmonics are sufficient to adequately describe the observed pulse profile; i.e., they yield $\chi^2_\nu \approx 1.0$ and including higher harmonics does not significantly improve the fit. This is expected, as the thermal pulsations are relatively broad and smooth and the MSPs under consideration are not in a regime of NS spins where rapid rotation introduces strong higher harmonics. The residuals of the four harmonic fits do not show any broad residuals, statistically significant narrow features, or enhanced variance compared to what is expected.

8. Phase-selected Spectroscopic Analysis

Previous analyses of the four MSPs have shown that their X-ray continua can be well described by a predominantly thermal spectrum (blackbody or NS atmosphere), with a requirement for more than one temperature for PSRs J0437−4715 (Zavlin 2006; Bogdanov 2013) and J0030+0451 (Bogdanov & Grindlay 2009). For these two MSPs, above ∼3 keV, a power-law tail is seen in the spectrum. It is important to note that there are limitations to standard phase-resolved spectroscopy, compared to the full phase-channel inference analyses used in Miller et al. (2019b) and Riley et al. (2019). For instance, the rotation of the NS and associated spin-phase flux averaging, as well as the relativistic effects and detailed geometry of the system, such as the location of the hot regions on the surface and the observer viewing angle, are not taken into consideration. In addition, the NS atmosphere models available in XSPEC (Arnaud 1996) are constructed based on the assumption of uniform radiation from the entire surface of an NS but the emergent intensity of an NS atmosphere has a strong dependence on the emission angle (see, e.g., Zavlin et al. 1996). Moreover, even at pulse maximum the emitting region may not be viewed face-on. As a consequence, the inferred temperatures and radii of the hot spots may significantly deviate from the true values. Nevertheless, phase-resolved spectroscopy can still provide useful insight regarding the general properties of the surface radiation.

With these caveats in mind, we conducted phase-resolved spectroscopic analyses of these pulsars by selecting relatively narrow phase intervals around the peaks in the pulse profiles.

[30] The non-spot background (i.e., emission that does not originate from the surface hot spots such as instrumental and sky backgrounds and nonthermal X-rays from the environment around the pulsar) is treated in the same manner in the inference analyses for PSR J0030+0451 presented in Miller et al. (2019b) and Riley et al. (2019).

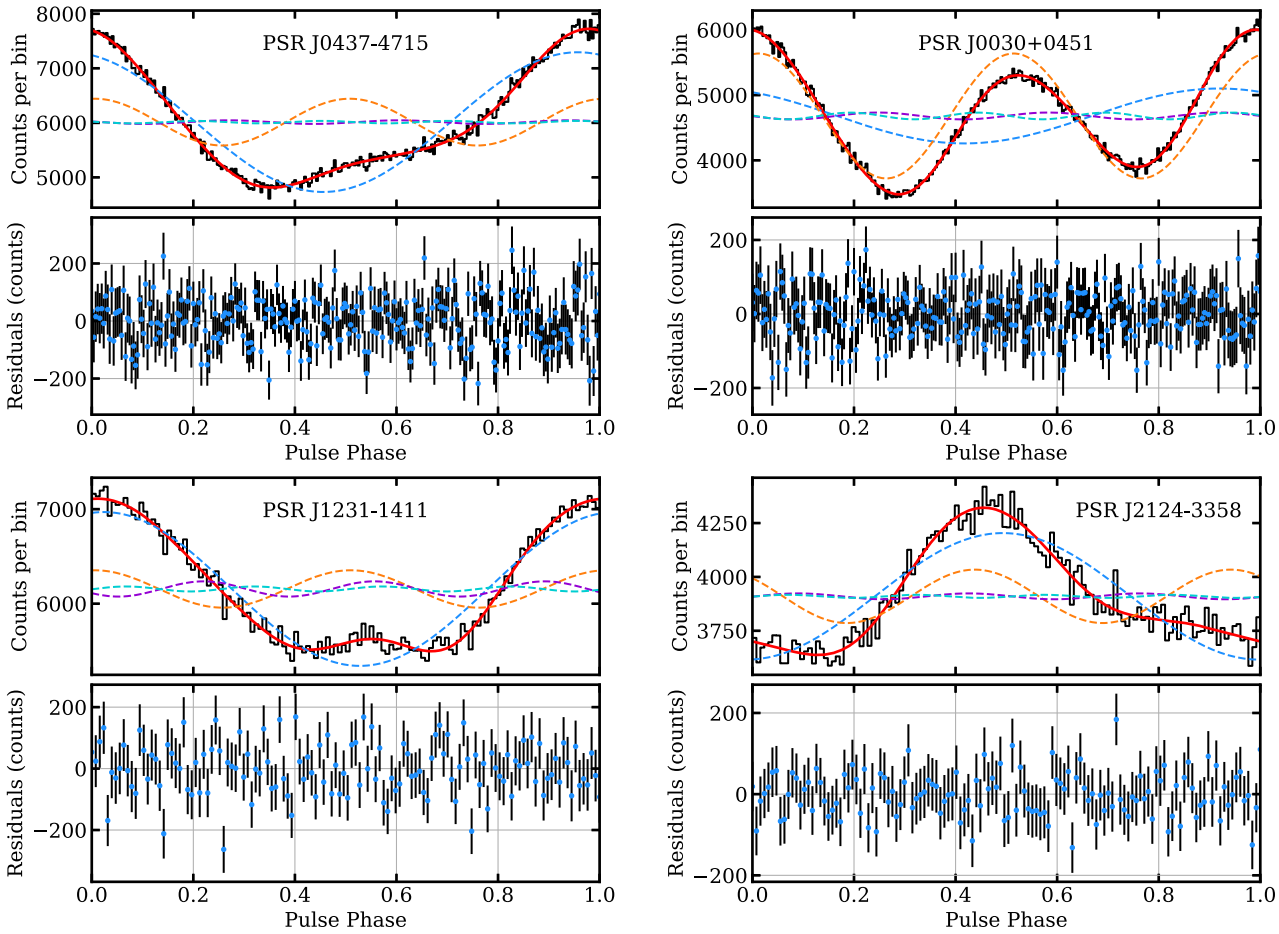

Figure 5. Folded *NICER* XTI profiles from Figure 2 but grouped in 256 (for PSRs J0437−4715 and J0030+0451) or 128 phase bins (for PSRs J1231−1411 and J2124−3358). The solid red lines show the best fit with a model of the profile constructed from the empirical Fourier coefficients, given by Equation (1), of the set of photon phases. The dashed lines show the sinusoids corresponding to the first four harmonic components of the fit (blue, orange, purple, and cyan for the first, second, third, and fourth harmonic, respectively). The bottom panel for each pulsar shows the residuals from the fit.

Such phase selections (see Figure 2) permit focusing on a single hot spot at a time, while also minimizing phase averaging. The spectra are therefore extracted within $\Delta\phi = 0.2$ phase intervals around the peaks. For each pulsar, a model of the background is generated from the COR_SAX and K_p parameters of the GTIs used, with the space-weather-based technique described in Section 4. The event file filtering differs from that used for the full phase-channel analyses, and was optimized to produce the best match to the background model. For example, the minimum COR_SAX value was set to 1.0 for PSR J2124−3358, PSR J1231−1411, and PSR J0437−4715, while it was maintained at 1.5 for PSR J0030+0451. These empirically produced background models provided a better match to the observed spectra above 3 keV, where the non-source emission dominates above the pulsar flux.

The spectrum used to model thermal emission is that of the NS hydrogen atmosphere model `nsatmos` (Heinke et al. 2006) in XSPEC, where one, two, or three such components were added when needed. For each `nsatmos` component, we fit for the temperatures and normalizations (equivalent to the fraction of the total NS surface) and we fix the distances, masses, and radii, either to the known values when available or to canonical values. Absorption due to the interstellar Galactic medium is modeled with `tbabs`, which employs the VERN cross-sections (Verner et al. 1996) and WILM abundances (Wilms et al. 2000). For each pulsar, the two peaks are fit simultaneously, keeping only the absorption parameter $N_{\rm H}$ tied between the two spectra. For PSR J1231−1411, a Gaussian component was added to account for excess of counts near the 0.57 keV O VII emission line, as observed in the phase-averaged analysis presented in Ray et al. (2019), and probably caused by Solar wind charge exchange or originating in the local hot bubble (Kuntz 2019). The other three pulsars do not exhibit such spectral features, likely due to weaker contamination from charge exchange along those lines of sight. Finally, we added a 3% systematic to account for uncertainties in the background modeling. We note that in all cases but PSR J0437−4715, the backgrounds represent $\gtrsim$50% of the total extracted counts in the bands used, and as much as ∼80% for PSR J2124−3358. Uncertainties in the modeling of the background spectra can have important effects on the pulsar spectral analyses (see Section 4 for details). The results for each target are presented in the following subsections and the best-fit models to the spectral data are displayed in Figure 6.

8.1. PSR J0437−4715

In the analysis of PSR J0437−4715, the following parameters of each `nsatmos` spectral component are kept fixed: $M = 1.44\ M_\odot$ and $D = 156.79$ pc, because they are precisely and independently measured (Reardon et al. 2016). Neither

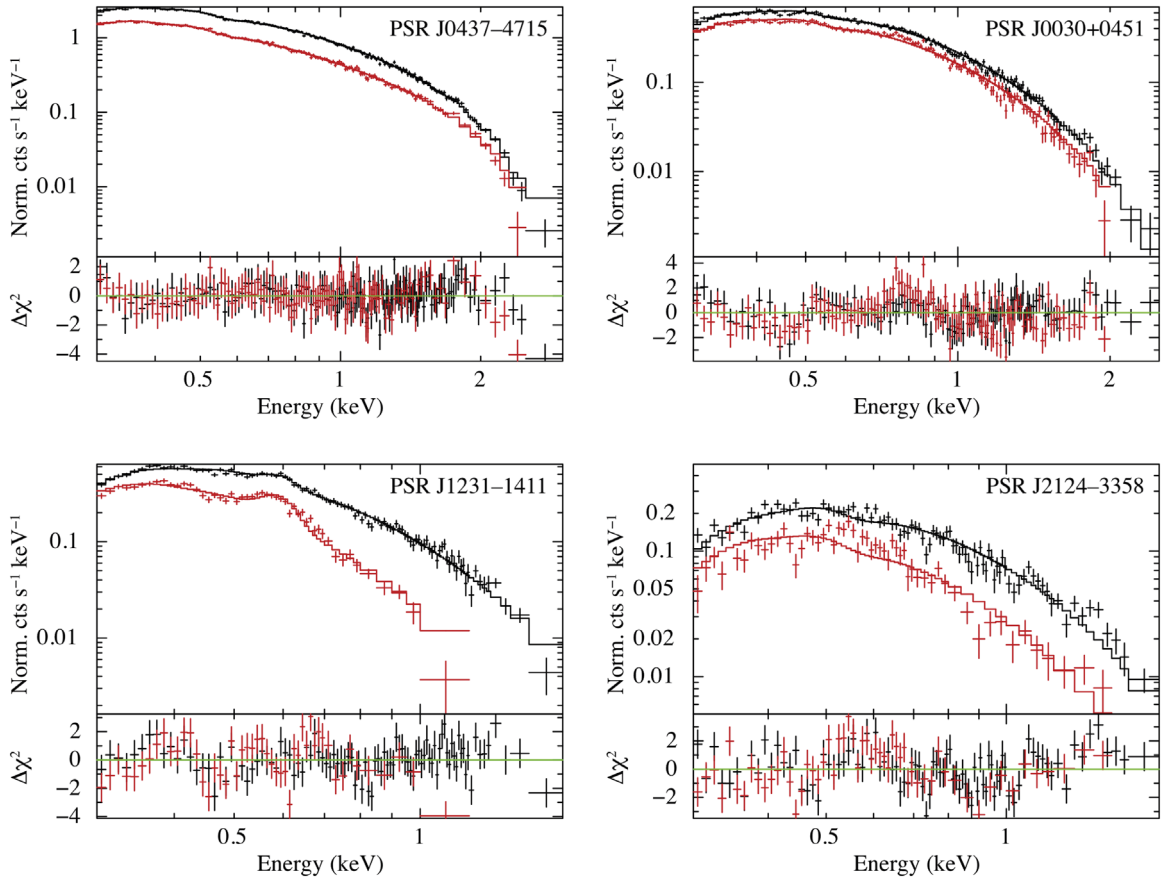

Figure 6. Folded spectra of the two peaks of all four pulsars. In each panel, the dominant peak (peak 1) is represented in black and the secondary peak (peak 2) is in red. The bottom panel of each figure shows the residuals to the best-fit model in Tables 3–6.

single-nsatmos nor double-nsatmos spectral models describe the data well ($\chi^2 = 6806.81$ for 258 d.o.f., and $\chi^2 = 394.17$ for 254 d.o.f., respectively). As was observed in previous phase-averaged analyses of this pulsar, three thermal components are necessary to model the observed emission. The coldest nsatmos component is expected to emerge from the entire surface of the NS (Durant et al. 2012; Bogdanov 2013; Guillot et al. 2016; Gonzalez-Caniulef et al. 2019), and is therefore expected to be visible at all phases. Therefore, each spectrum studied here (one for each peak) likely displays the emission from a two-temperature polar cap in addition to the emission from the entire surface, the latter assumed to be the same for each peak (although with different effective emission areas).

For this reason, we choose to keep the parameters of the cold nsatmos surface component tied between the spectra of the two peaks, except for their normalizations, which are constrained to be equal to 1 minus the normalizations of the other two nsatmos components for the same peak. As a result, the cold nsatmos normalizations are not degenerate with the NS radius, which can then be a free parameter. We can therefore fit the NS radius at the same time as the parameters from the hot polar caps emission. Although this does not have the robustness of a full phase-energy-resolved analysis, the results, presented in Table 3, can be informative.

We find that the nsatmos2 (mid-temperature) component has comparable temperatures in both peaks. However, the nsatmos3 (high-temperature) component appears hotter in the second (less-prominent) peak. As expected from their contributions to the total pulse profile, the second peak has smaller nsatmos2 and nsatmos3 normalizations, indicating a polar cap that is either smaller than that of peak 1, or is viewed at a larger angle by the observer. This ought to be clarified from detailed modeling of the phase-energy-resolved data (as described in Miller et al. 2019b and Riley et al. 2019), which will be presented in subsequent publications. The best-fit temperature and radius of the coldest nsatmos component (nsatmos1) have to be interpreted with care. Indeed, its contribution to the total spectrum is minimal (as it peaks outside the *NICER* band) and it is only constrained at the lowest energies where contamination from optical loading may still be present, even when considering Sun angles $>80^\circ$ (see Section 4). We note that in this spectroscopic analysis the NS radius is not well constrained primarily because it does not take into account the full three-dimensional geometry and rotation of the system. Therefore, it is not as nearly as sensitive to the NS radius as a full inference analysis that considers the energy-dependent beaming pattern of the NS atmosphere, gravitational bending of light, viewing geometry, and stellar rotation. In addition, due to the way that the nsatmos model is parameterized, the NS radius and the flux normalization are covariant, which increases the uncertainty in R.

8.2. PSR J0030+0451

In the spectral analysis of PSR J0030+0451, we fix the NS radius and mass parameters to $R = 12.7$ km and $M = 1.34\ M_\odot$ (from Riley et al. 2019), as well as the distance $d = 325$ pc—but we note that the fit is not very sensitive to small variations of M

Table 3
Results of the *NICER* Spectral Analysis for PSR J0437−4715

Component	Parameter	Peak 1	Peak 2
tbabs	$N_{\rm H}$ (10^{20} cm^{-2})	$0.08\ ^{+0.20}_{-0.08}$	
nsatmos1	$\log T_{\rm eff}$	$5.26^{+0.05}_{-0.18}$	
	M ($M_\odot$)	(1.44)	
	R (km)	$15.3\ ^{+2.0}_{-1.6}$	
	D (pc)	(156.79)	
	Norm.	$1.0 - (N_2 + N_3)$	$1.0 - (N_2 + N_3)$
nsatmos2	$\log T_{\rm eff}$	$5.71^{+0.05}_{-0.05}$	$5.74^{+0.05}_{-0.05}$
	Norm. N_2	$0.036^{+0.018}_{-0.012}$	$0.021^{+0.012}_{-0.008}$
nsatmos3	$\log T_{\rm eff}$	$6.23^{+0.02}_{-0.01}$	$6.29^{+0.03}_{-0.02}$
	Norm. N_3	$0.00035^{+0.00011}_{-0.00008}$	$0.00009^{+0.00003}_{-0.00002}$
Count rate (s^{-1})		1.509	0.887
$F_{0.3-2.0\ \rm keV}$ (10^{-13} erg cm^{-2} s^{-1})		15.78 ± 0.05	9.28 ± 0.05
$L_{0.3-2.0\ \rm keV}$ (10^{30} erg s^{-1})		4.64 ± 0.01	2.73 ± 0.01
χ^2_ν (d.o.f.)		0.84 (252)	

Note. Values in parentheses are kept fixed. Due to the complex shape of the parameter space, errors were estimated from a Markov Chain Monte Carlo within XSPEC (500,000 iterations, with 100 walkers). Reported values correspond to the 50% quantiles, and the upper/lower uncertainties are the 5% and 95% quantiles so that they represent the 90% credible intervals. A multiplicative constant with fixed value of 0.95 was used to account for the 1.″5 offset pointing (see Figure 7).

Table 4
Results of the *NICER* Spectral Analysis for PSR J0030+0451

Component	Parameter	Peak 1	Peak 2
tbabs	$N_{\rm H}$ (10^{20} cm^{-2})	$0.03\ ^{+0.25}_{-0.03}$	
nsatmos	$\log T_{\rm eff}$	$6.036^{+0.004}_{-0.007}$	$6.014^{+0.005}_{-0.007}$
	M ($M_\odot$)	(1.34)	
	R (km)	(12.7)	
	D (pc)	(325)	
	Norm.	$0.0055^{+0.0005}_{-0.0002}$	$0.0052^{+0.0005}_{-0.0003}$
Count rate (s^{-1})		0.405	0.312
$F_{0.3-2.0\ \rm keV}$ (10^{-13} erg cm^{-2} s^{-1})		3.78 ± 0.02	2.92 ± 0.02
$L_{0.3-2.0\ \rm keV}$ (10^{30} erg s^{-1})		4.78 ± 0.02	3.69 ± 0.02
χ^2_ν (d.o.f.)		1.35 (250)	

Note. Values in parentheses are kept fixed. All errors reported are at 90% confidence.

and R, which can be absorbed in adjustments of the other parameters. We obtain a marginally acceptable fit with $\chi^2_\nu = 1.35$ (for 250 d.o.f.). The temperature and normalizations of the two peaks are reported in Table 4. Using the nominal best-fit values for $R = 13.02$ km and $M = 1.44\ M_\odot$ from Miller et al. (2019b) produces similar results.

Adding another nsatmos component (with smaller temperature) is not strictly required by the data.[31] Therefore, we report here the fit with only one thermal component. We find temperatures that are colder than those reported in Miller et al. (2019b) and Riley et al. (2019): $\log T_{\rm eff} \sim 6.11$ for both polar caps, Peak 1 corresponding to the crescent/oval and Peak 2 to the

[31] A simulation, using simftest in XSPEC finds a probability of 0.005 (not quite 3σ) that the additional component is required.

Table 5
Results of the *NICER* Spectral Analysis for PSR J1231−1411

Component	Parameter	Peak 1	Peak 2
tbabs	$N_{\rm H}$ (10^{20} cm^{-2})	1.7 ± 0.3	
Gaussian	$E_{\rm G}$ (keV)	$0.590^{+0.005}_{-0.001}$	
	$\sigma_{\rm G}$ (keV)	$(1.5 \pm 0.2) \times 10^{-5}$	
	Norm (10^{-5} ph cm^{-2} s^{-1})	$(1.3 \pm 0.2) \times 10^{-5}$	
nsatmos	$\log T_{\rm eff}$	$5.85^{+0.01}_{-0.01}$	$5.63^{+0.02}_{-0.02}$
	M ($M_\odot$)	(1.4)	
	R (km)	(11.0)	
	D (pc)	(420)	
	Norm.	$0.075^{+0.014}_{-0.011}$	$0.48^{+0.13}_{-0.10}$
Count rate (s^{-1})		0.27	0.13
$F_{0.3-2.0\ \rm keV}$ (10^{-13} erg cm^{-2} s^{-1})		2.56 ± 0.02	$1.28^{+0.01}_{-0.03}$
$L_{0.3-2.0\ \rm keV}$ (10^{30} erg s^{-1})		5.40 ± 0.05	$2.70^{+0.02}_{-0.06}$
χ^2_ν (d.o.f.)		1.49 (141)	

Note. Values in parentheses are kept fixed. All errors reported are at 90% confidence.

Table 6
Results of the *NICER* Spectral Analysis for PSR J2124−3358

Component	Parameter	Peak 1	Peak 2
tbabs	$N_{\rm H}$ (10^{20} cm^{-2})	$3.1\ ^{+0.8}_{-0.8}$	
nsatmos	$\log T_{\rm eff}$	5.99 ± 0.02	5.88 ± 0.03
	M ($M_\odot$)	(1.4)	
	R (km)	(11.0)	
	D (pc)	(410)	
	Norm.	$0.008^{+0.003}_{-0.002}$	$0.014^{+0.006}_{-0.005}$
Count rate (s^{-1})		0.130	0.063
$F_{0.3-2.0\ \rm keV}$ (10^{-13} erg cm^{-2} s^{-1})		$1.27^{+0.01}_{-0.04}$	$0.62^{+0.01}_{-0.03}$
$L_{0.3-2.0\ \rm keV}$ (10^{30} erg s^{-1})		$2.54^{+0.02}_{-0.06}$	$1.26^{+0.02}_{-0.06}$
χ^2_ν (d.o.f.)		1.92 (142)	

Note. Values in parentheses are kept fixed. All errors reported are at 90% confidence. A multiplicative constant with fixed value of 0.98 was used to account for the 1′ offset pointing (see Figure 7).

circular spot in the favored models reported in those papers. The difference between the temperatures of Table 4 and those in Miller et al. (2019b) and Riley et al. (2019) can be attributed to a combination of the present analysis considering spectra averaged over 0.2 in pulse phase, not fully accounting for the viewing geometry of the system and all relevant general and special relativistic effects, and the use of atmosphere model spectra integrated over all angles.

8.3. PSR J1231−1411

A phase-averaged spectral analysis of a 916 ks subset of the data studied in the present Letter has been performed in the article summarizing the discovery of pulsations from this pulsar (Ray et al. 2019). The authors concluded that a double-blackbody model (with temperatures 44 and 133 eV) or a single NS hydrogen atmosphere model with effective temperature 51 eV was required to fit the data. Here we analyze the enlarged data set for PSR J1231−1411, i.e., 1320 ks of good time after optimal filtering for the spectral analysis. Since the two peaks are separated into two spectra, a single nsatmos component is fitted to each, assuming $M = 1.4\ M_\odot$ and

$R = 11$ km. The assumed value of R is based on existing measurements from quiescent NS X-ray binaries (see, e.g., Steiner et al. 2018, and references therein); choosing a different value does not change the main conclusions of the analysis. As with the other pulsars, only the absorption parameter $N_{\rm H}$ is tied between the two peaks. Furthermore, as was found in Ray et al. (2019), an O VII line feature is necessary to fit the thermal spectrum of this pulsar (the line parameters are also tied between the two spectra). We find `nsatmos` effective temperatures corresponding to 61 eV and 37 eV for the two peaks, respectively. Results are presented in Table 5.

8.4. PSR J2124−3358

PSR J2124−3358 is the faintest of the four pulsars presented here. The results of its spectral analysis are somewhat uncertain and dependent on the reliability of the background model. Indeed, the pulsar count rates represent only 24% and 15% of the total counts for the spectra of the dominant peak and secondary peak, respectively, in the 0.3–1.5 keV band. We again assume fixed values of $M = 1.4\ M_{\odot}$ and $R = 11$ km. The analysis, similar to the other pulsars described above, finds the dominant peak with a higher temperature but smaller size (although not significantly) than the secondary peak (Table 6). These findings are qualitatively consistent with those of Bogdanov et al. (2008), if the two thermal components used in that work are assumed to originate from the two peaks in the pulse profile as studied here.

Finally, we note that the cold emission from the entire pulsar surface ($T_{\rm BB} = (0.5\text{–}2.1) \times 10^5$ K; see Rangelov et al. 2017) measured in the far-UV with the *Hubble Space Telescope* remains mostly outside the *NICER* band, and therefore cannot be detected (unlike for PSR J0437−4715).

9. Conclusions

In this Letter we have presented the deep *NICER* data sets of PSRs J0437−4715, J0030+0451, J1231−1411, and J2124−3358, the four rotation-powered MSPs we have selected for analysis aimed at constraining the NS *M*–*R* relation and the dense matter EoS. The data were reduced using the best available tools and data cleaning techniques the *NICER* team has developed. The substantial increase in photon statistics of these data compared to previous observations of these targets enables better characterization of their pulsed emission. We examined the timing behavior, long-term variability, Fourier-domain characteristics, and spectral properties of the event data.

We confirm that the superb absolute timing capabilities of *NICER* enable folding of the event data, spanning 1.5–2 yr, coherently with the radio ephemerides with virtually no pulse smearing. We find that the pulsed emission does not exhibit significant changes over the observing span, as expected from polar cap emission from rotation-powered MSPs. A Fourier decomposition of the folded events shows that four harmonics are sufficient to fully describe the broad thermal pulsations and the folded profiles have the expected statistical properties. Our phase-resolved spectroscopic analyses yield results generally consistent with previous results.

Overall, we find that the *NICER* data of the four MSPs do not exhibit any anomalies and are thus suitable for detailed inference analyses. The *NICER* data for PSR J0030+0451 presented here[32] are used in Miller et al. (2019b) and Riley et al. (2019) to obtain estimates on *M* and *R* through principled Bayesian inference analyses. In Miller et al. (2019b), constraints are presented on the dense matter EoS, as well, while in Raaijmakers et al. (2019), the *M*–*R* constraints from Riley et al. (2019) are used to provide estimates on the properties of cold, dense matter. Similar investigations for the other three MSPs are ongoing and will be presented in subsequent publications.

This work was supported by NASA through the *NICER* mission and the Astrophysics Explorers Program. A portion of the analysis presented was based on archival observations obtained with *XMM-Newton*, an ESA science mission with instruments and contributions directly funded by ESA Member States and NASA. S.G. acknowledges the support of the Centre National d'Études Spatiales (CNES). A.L.W. and T.E.R. acknowledge support from ERC Starting grant No. 639217 CSINEUTRONSTAR (PI: Watts). M.C.M. is grateful for the hospitality of Perimeter Institute where part of this work was carried out. Research at Perimeter Institute is supported in part by the Government of Canada through the Department of Innovation, Science and Economic Development Canada and by the Province of Ontario through the Ministry of Economic Development, Job Creation and Trade. This research has made use of data and software provided by the High Energy Astrophysics Science Archive Research Center (HEASARC), which is a service of the Astrophysics Science Division at NASA/GSFC and the High Energy Astrophysics Division of the Smithsonian Astrophysical Observatory. We acknowledge extensive use of NASA's Astrophysics Data System (ADS) Bibliographic Services and the ArXiv.

Facilities: NICER, *XMM-Newton*.

Software: `HEAsoft` (Nasa High Energy Astrophysics Science Archive Research Center (Heasarc), 2014), `Tempo2` (Hobbs et al. 2006), `PINT` (https://github.com/nanograv/pint), `XSPEC` (Arnaud 1996), `NICERSoft` (https://github.com/paulray/NICERsoft).

Appendix
Background Sources Near the Targets and *NICER* Pointing Optimization

For each pulsar, we calculate the optimal pointing position based on the method described below. The goal is to maximize

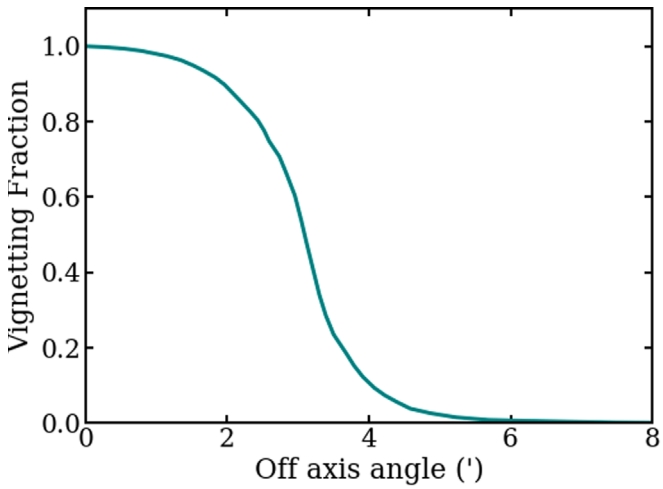

Figure 7. *NICER* vignetting curve estimate based on ray tracing showing the fraction of flux received as a function of off-axis angle.

[32] The filtered and phase-folded event data set for PSR J0030+0451 is provided on Zenodo (doi:10.5281/zenodo.3524457).

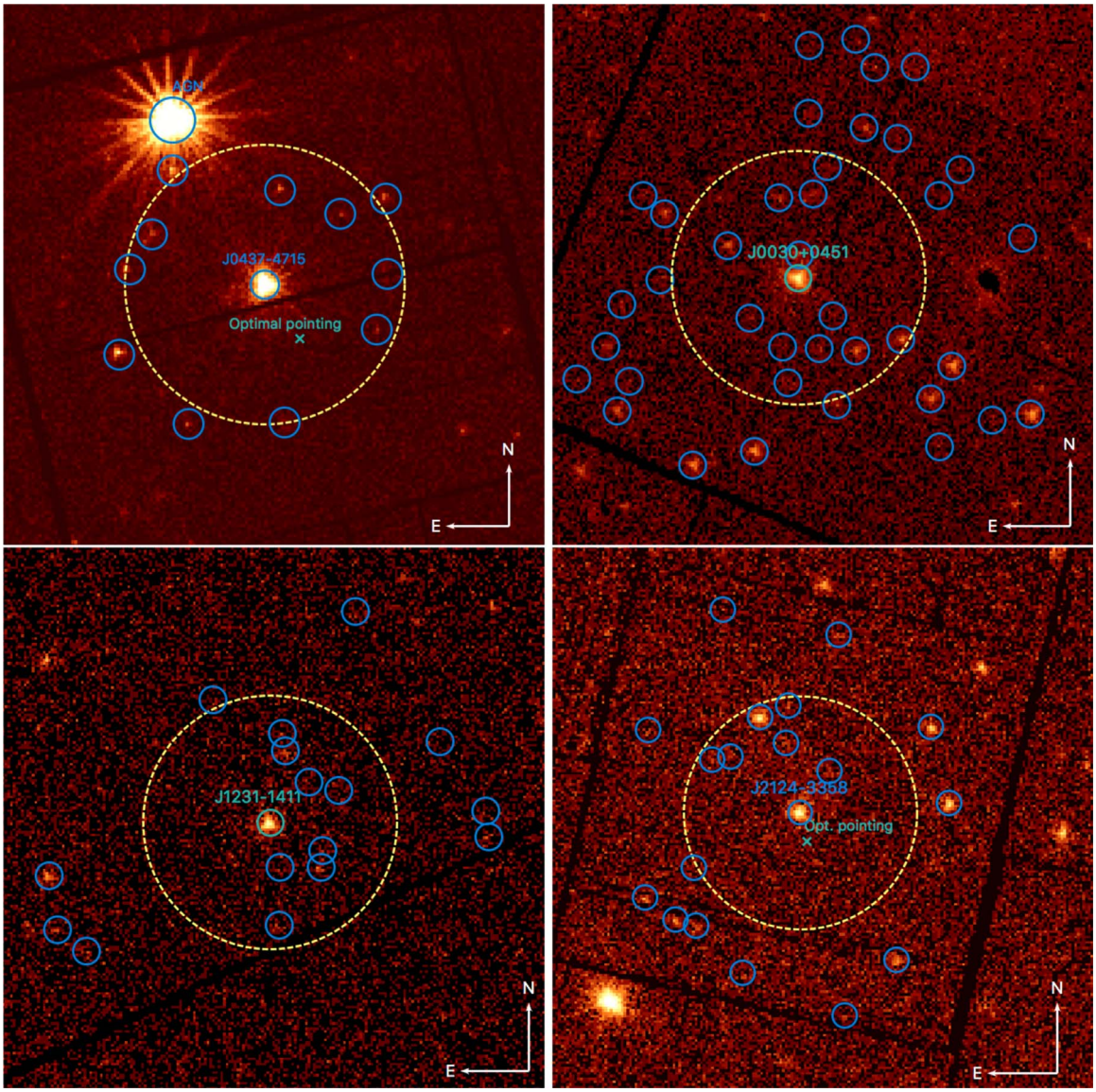

Figure 8. *XMM-Newton* EPIC MOS1/2 images of PSRs J0437−4715 (top left), J0030+0451 (top right), J1231−1411 (bottom left), and J2124−3358 (bottom right) and nearby sources marked with blue circles. The large dashed yellow circle indicates the *NICER* point-spread function with half-power diameter of 6′.2. For PSRs J0437−4715 and J2124−3358, the teal "×" shows the position of the optimal *NICER* pointing that maximizes the S/N from the pulsar, i.e., minimizes the contamination from surrounding sources. For the other two pulsars, PSRs J0030+0451 and J1231−1411, the optimal pointing distance from the pulsar and the gain in S/N are negligible.

the S/N from the pulsar, defined as

$$\mathrm{S/N} = \frac{C_{\mathrm{PSR}} \times t_{\mathrm{exp}}}{\sqrt{t_{\mathrm{exp}} \times \left(C_{\mathrm{PSR}} + \sum_i C_i + C_{\mathrm{BKG}}\right)}}, \quad (3)$$

by minimizing the contributions C_i from nearby sources, while keeping the pulsar count rate C_{PSR} as large as possible. C_{BKG} corresponds to the non-astrophysical (particle and instrumental) background assumed to be constant, and t_{exp} is the exposure time. The vignetting function of *NICER* remains relatively flat within $\sim 2'$ of the aimpoint, but drops sharply at distance $\gtrsim 3'$ from the aimpoint (see Figure 7, which shows the pre-launch estimate based on ray tracing). The optimal pointing method therefore naturally attempts keeping the brightest nearby source outside $\sim 2'$–$3'$ while maintaining the pulsar within $<2'$ of the aimpoint.

Since all the pulsars presented in this Letter have been observed with the imaging MOS detectors of *XMM-Newton* (Figure 8), fluxes and spectral information in the soft X-ray band exist for all nearby sources. We make use of the 3XMM-DR8 Catalog (Rosen et al. 2016) to estimate the nominal *NICER* count rate of nearby sources (i.e., if they were placed at the aimpoint). Cataloged sources with $F_{\mathrm{X}} \gtrsim 1 \times 10^{-14}\,\mathrm{erg\,s^{-1}\,cm^{-2}}$ can be fit with the online spectral fitting tools of the 3XMM-DR8 Catalog.[33] For these, we fit the spectrum with simple models (absorbed power-law or thermal models), and use the best fit parameters in WebPIMMS to estimate their *NICER* count rates. For the fainter sources, when the online spectral fitting tool is not

[33] Available at http://xmm-catalog.irap.omp.eu.

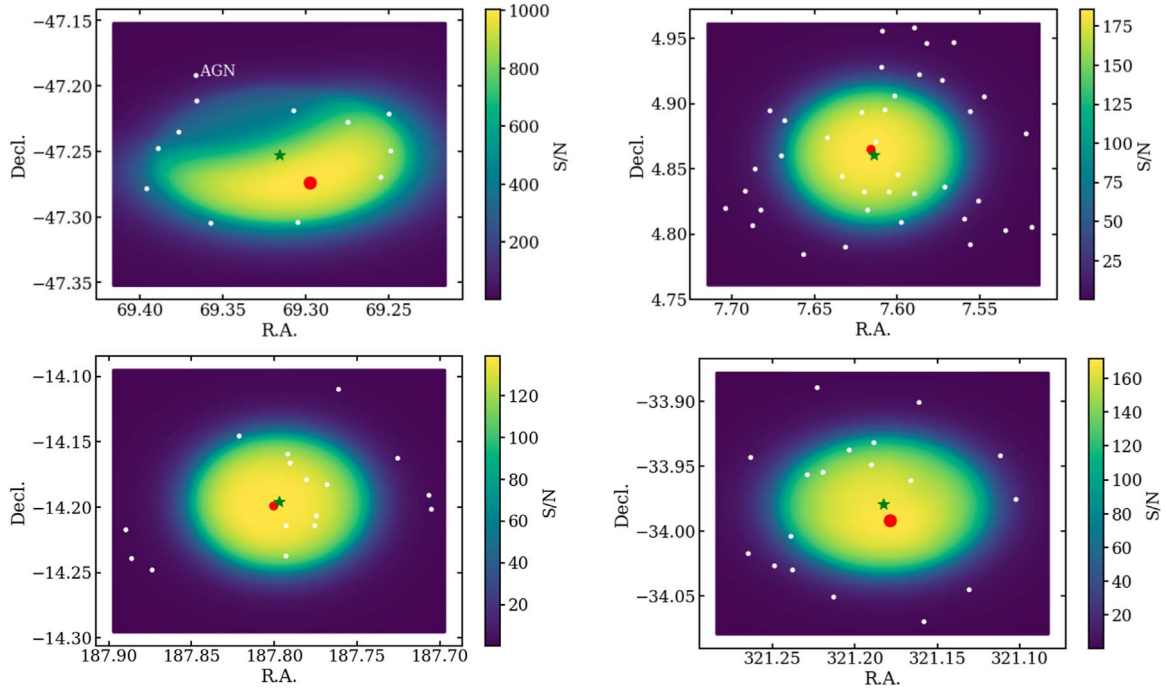

Figure 9. Maps of the S/N of PSRs J0437−4715 (top left), J0030+0451 (top right), J1231−1411 (bottom left), and J2124−3358 (bottom right) as a function of the *NICER* pointing as a function of the *NICER* pointing, for $t_{\rm exp} = 10^6$′s (see Equation (3)). The green star indicates the pulsar position, and the red circle shows the calculated optimal pointing position that maximizes the S/N. For PSRs J0437−4715, the pointing offset is 1.′5 from the pulsar to minimize contamination by the active galactic nucleus RX J0437.4−4711, and for PSR J2124−3358 the pointing offset is 1′.

Table 7
Other X-Ray Sources Near PSR J0437–4715

Name	$F_{0.2-10\ \rm keV}$ ($\times 10^{-14}$ erg s^{-1} cm^{-2})	*NICER* Count Rate (s^{-1})	Distance from PSR (arcmin)	Vignetting Fraction	Scaled *NICER* Count Rate (s^{-1})	Count Rate at Optimal Pointing (s^{-1})
3XMM J043728.1−471129 (AGN)	1300	9.577	4.18	0.07	0.7629	0.0768
3XMM J043735.1−471638	6.4	0.037	3.62	0.21	0.0075	0.0038
3XMM J043728.0−471237	3.1	0.021	3.20	0.42	0.0088	0.0007
3XMM J043734.1−471448	3.2	0.007	2.99	0.50	0.0040	0.0007
3XMM J043730.6−471400	2.9	0.019	2.70	0.68	0.0136	0.0020
3XMM J043705.9−471336	2.5	0.003	2.25	0.83	0.0025	0.0018
3XMM J043700.0−471454	2.5	0.009	2.73	0.71	0.0064	0.0071
3XMM J043701.3−471609	2.3	0.002	2.69	0.72	0.0014	0.0019
3XMM J043713.3−471812	1.6	0.006	3.14	0.50	0.0028	0.0055
3XMM J043700.4−471313	1.4	0.011	3.27	0.34	0.0041	0.0020
3XMM J043725.9−471814	1.2	0.006	3.56	0.24	0.0013	0.0032
3XMM J043714.0−471301	1.1	0.013	2.06	0.87	0.0114	0.0040

available, we simply convert the 0.2–10 keV reported in the catalog to a *NICER* count rate assuming a $\Gamma = 2$ power-law model.

Using the vignetting function for *NICER*, the actual observed count rate of each source is calculated given its distance from the aimpoint. With these, we can perform a grid search of alternative pointing around the pulsar to search for that which will maximize the S/N for the pulsar, i.e., which will minimize the contamination from nearby sources without decreasing too much the count rate of the pulsar.[34] Figure 9 shows the maps of S/N for different pointing around the pulsars, as well as the positions of nearby sources, and the position of the optimal pointing resulting from the grid search described above.

For PSR J0437−4715, we only include sources within 6′ and $F > 1 \times 10^{-14}$ erg s^{-1} cm^{-2}; fainter sources will have a negligible contributions for the purpose of optimizing the pointing as the pulsar flux is $F \approx 1 \times 10^{-12}$ erg s^{-1} cm^{-2}. Table 7 summarizes the properties and count rates of these nearby sources. The AGN RX J0437.4−4711 dominates the S/N map, and the optimal pointing is naturally in the direction opposite to the AGN position. For all other pulsars, we considered all sources within 6′ of the targets. Tables 8–10 present the properties of the nearby sources, and the S/N maps is displayed in Figure 9.

[34] The code is available here: https://github.com/sguillot/NICER.

Table 8
Other X-Ray Sources Near PSR J0030+0451

Name	$F_{0.2-10\ \mathrm{keV}}$ ($\times 10^{-14}$ erg s^{-1} cm^{-2})	*NICER* Count Rate (s^{-1})	Distance from PSR (arcmin)	Vignetting Fraction	Scaled *NICER* Count Rate (s^{-1})	Count Rate at Optimal Pointing (s^{-1})
3XMM J003027.2+045214	1.00	0.004	0.59	0.99	0.004	0.004
3XMM J003023.9+045044	0.43	0.002	1.27	0.96	0.002	0.002
3XMM J003032.0+045041	0.27	0.001	1.51	0.93	0.001	0.001
3XMM J003028.8+044958	0.91	0.004	1.73	0.91	0.003	0.004
3XMM J003025.2+044956	1.04	0.004	1.80	0.91	0.004	0.003
3XMM J003034.2+045227	1.22	0.005	1.87	0.90	0.006	0.005
3XMM J003029.2+045337	1.37	0.006	2.01	0.89	0.005	0.006
3XMM J003025.8+045343	0.71	0.003	2.10	0.86	0.003	0.003
3XMM J003021.6+044953	2.38	0.010	2.28	0.80	0.008	0.008
3XMM J003028.3+044906	0.79	0.003	2.56	0.71	0.002	0.002
3XMM J003024.4+045423	0.74	0.003	2.83	0.62	0.002	0.002
3XMM J003017.2+045010	3.17	0.013	2.95	0.58	0.008	0.006
3XMM J003023.5+044834	0.47	0.002	3.24	0.45	0.001	0.0005
3XMM J003040.8+045137	0.76	0.003	3.35	0.40	0.001	0.001
3XMM J003040.4+045314	3.81	0.016	3.62	0.28	0.004	0.005
3XMM J003013.5+045340	2.17	0.009	4.00	0.11	0.001	0.001
3XMM J003020.8+045520	1.50	0.006	4.03	0.11	0.001	0.0008
3XMM J003026.3+045541	0.56	0.002	4.03	0.11	0.0002	0.0003
3XMM J003017.5+045504	1.08	0.004	4.21	0.09	0.0004	0.0004
3XMM J003042.5+045341	0.44	0.002	4.28	0.08	0.0002	0.0002
3XMM J003012.2+044931	5.83	0.024	4.35	0.08	0.002	0.0009
3XMM J003044.6+045101	0.23	0.001	4.35	0.08	0.0001	0.00007
3XMM J003031.6+044726	4.21	0.017	4.35	0.08	0.001	0.0007
3XMM J003014.3+044843	2.84	0.012	4.39	0.07	0.001	0.0004
3XMM J003011.4+045419	0.28	0.001	4.79	0.04	0.0001	0.00003
3XMM J003043.8+044908	0.34	0.001	4.82	0.04	0.0001	0.00003
3XMM J003046.1+044959	0.92	0.004	4.95	0.02	0.0001	0.00009
3XMM J003037.6+044705	3.34	0.014	5.23	0.02	0.0003	0.0002
3XMM J003013.4+044732	0.43	0.002	5.39	0.02	0.00003	0.00002
3XMM J003045.0+044825	2.95	0.012	5.46	0.02	0.0002	0.0001
3XMM J003019.8+045648	0.19	0.001	5.49	0.02	0.00001	0.00001
3XMM J003005.3+045238	0.26	0.001	5.57	0.01	0.00002	0.00001
3XMM J003026.2+045721	0.74	0.003	5.70	0.01	0.00004	0.00003
3XMM J003008.3+044811	0.30	0.001	5.88	0.01	0.00001	0.00001
3XMM J003015.8+045649	2.66	0.011	5.91	0.01	0.0001	0.00008
3XMM J003049.0+044911	0.26	0.001	5.93	0.01	0.00001	0.00001
3XMM J003021.6+045729	1.26	0.005	6.00	0.01	0.00003	0.00004
3XMM J003004.5+044820	8.13	0.034	6.61	0.01	0.0001	0.0001

Table 9
Other X-Ray Sources Near PSR J1231–1411

Name	$F_{0.2-10\ \mathrm{keV}}$ ($\times 10^{-14}$ erg s^{-1} cm^{-2})	*NICER* Count Rate (s^{-1})	Distance from PSR (arcmin)	Vignetting Fraction	Scaled *NICER* Count Rate (s^{-1})	Count Rate at Optimal Pointing (s^{-1})
3XMM J123110.3−141249	0.55	0.002	1.12	0.97	0.0022	0.0020
3XMM J123107.4−141044	0.76	0.003	1.36	0.95	0.0030	0.0028
3XMM J123106.0−141224	0.50	0.002	1.45	0.94	0.0019	0.0019
3XMM J123106.2−141249	2.68	0.011	1.65	0.92	0.0104	0.0102
3XMM J123109.8−140958	2.67	0.011	1.78	0.91	0.0102	0.0097
3XMM J123104.4−141056	5.00	0.021	1.85	0.90	0.0190	0.0180
3XMM J123110.1−140933	0.38	0.002	2.19	0.83	0.0013	0.0016
3XMM J123110.4−141414	1.02	0.004	2.52	0.72	0.0031	0.0029
3XMM J123117.1−140843	0.68	0.003	3.32	0.42	0.0012	0.0008
3XMM J123054.2−140945	0.74	0.003	4.57	0.06	0.0002	0.00008
3XMM J123049.6−141126	1.16	0.005	5.25	0.02	0.0001	0.00006
3XMM J123049.3−141204	1.90	0.008	5.34	0.02	0.0001	0.00008
3XMM J123129.8−141452	0.79	0.003	5.50	0.02	0.0001	0.00005
3XMM J123102.7−140634	1.85	0.008	5.55	0.01	0.0001	0.00006
3XMM J123133.6−141301	3.18	0.013	5.56	0.01	0.0002	0.00016
3XMM J123132.7−141420	1.34	0.006	5.81	0.01	0.0001	0.00006

Table 10
Other X-Ray Sources Near PSR J2124–3358

Name	$F_{0.2-10\ \mathrm{keV}}$ ($\times 10^{-14}$ erg s^{-1} cm^{-2})	*NICER* Count Rate (s^{-1})	Distance from PSR (arcmin)	Vignetting Fraction	Scaled *NICER* Count Rate (s^{-1})	Count Rate at Optimal Pointing (s^{-1})
3XMM J212426.9−335629	4.11	0.026	4.15	0.08	0.0022	0.0010
3XMM J212424.6−335830	5.84	0.040	4.02	0.11	0.0042	0.0035
3XMM J212448.8−335613	11.2	0.033	2.76	0.71	0.0231	0.0091
3XMM J212431.3−340240	1.91	0.011	4.72	0.03	0.0004	0.0009
3XMM J212459.6−340135	1.70	0.007	4.30	0.06	0.0005	0.0009
3XMM J212503.5−340100	1.42	0.009	4.66	0.03	0.0003	0.0005
3XMM J212438.7−335401	0.97	0.005	4.84	0.03	0.0001	0.0001
3XMM J212457.0−340145	1.52	0.008	4.07	0.09	0.0008	0.0014
3XMM J212439.9−335739	1.27	0.007	1.37	0.96	0.0067	0.0063
3XMM J212452.6−335716	0.82	0.004	2.35	0.82	0.0037	0.0025
3XMM J212437.9−340409	1.37	0.008	5.53	0.01	0.0001	0.0002
3XMM J212445.5−335654	0.25	0.001	1.88	0.91	0.0013	0.0010
3XMM J212445.2−335554	0.42	0.002	2.86	0.65	0.0015	0.0005
3XMM J212454.9−335721	1.27	0.007	2.69	0.72	0.0050	0.0024
3XMM J212503.1−335633	0.36	0.002	4.57	0.04	0.0001	0.0000
3XMM J212453.5−335321	0.89	0.005	5.75	0.01	0.0000	0.0000
3XMM J212457.3−340013	0.52	0.003	3.15	0.45	0.0013	0.0014
3XMM J212451.0−340301	0.69	0.004	4.53	0.04	0.0002	0.0005

ORCID iDs

Slavko Bogdanov https://orcid.org/0000-0002-9870-2742
Sebastien Guillot https://orcid.org/0000-0002-6449-106X
Paul S. Ray https://orcid.org/0000-0002-5297-5278
Michael T. Wolff https://orcid.org/0000-0002-4013-5650
Deepto Chakrabarty https://orcid.org/0000-0001-8804-8946
Wynn C. G. Ho https://orcid.org/0000-0002-6089-6836
Matthew Kerr https://orcid.org/0000-0002-0893-4073
Frederick K. Lamb https://orcid.org/0000-0002-3862-7402
Renee M. Ludlam https://orcid.org/0000-0002-8961-939X
M. Coleman Miller https://orcid.org/0000-0002-2666-728X
Dimitrios Psaltis https://orcid.org/0000-0003-4058-2837
Thomas E. Riley https://orcid.org/0000-0001-9313-0493
James F. Steiner https://orcid.org/0000-0002-5872-6061
Tod E. Strohmayer https://orcid.org/0000-0001-7681-5845
Anna L. Watts https://orcid.org/0000-0002-1009-2354
Teruaki Enoto https://orcid.org/0000-0003-1244-3100
Craig B. Markwardt https://orcid.org/0000-0001-9803-3879

References

Abbott, B. P., Abbott, R., Abbott, T. D., et al. 2018, PhRvL, 121, 161101
Alpar, M. A., Cheng, A. F., Ruderman, M. A., & Shaham, J. 1982, Natur, 300, 728
Arnaud, K. A. 1996, in ASP Conf. Ser. 101, Astronomical Data Analysis Software and Systems V, ed. G. H. Jacoby & J. Barnes (San Francisco, CA: ASP), 17
Arzoumanian, Z., Brazier, A., Burke-Spolaor, S., et al. 2018, ApJS, 235, 37
Bailes, M., Johnston, S., Bell, J. F., et al. 1997, ApJ, 481, 386
Bailyn, C. D. 1993, ApJL, 411, L83
Bauswein, A., Stergioulas, N., & Janka, H.-T. 2016, EPJA, 52, 56
Becker, W., & Aschenbach, B. 2002, in Neutron Stars, Pulsars, and Supernova Remnants, ed. W. Becker, H. Lesch, & J. Trümper (Garching: Max-Planck-Institut für Extraterrestrische Physik), 64
Becker, W., & Trümper, J. 1993, Natur, 365, 528
Becker, W., & Trümper, J. 1999, A&A, 341, 803
Becker, W., Trümper, J., Lommen, A. N., & Backer, D. C. 2000, ApJ, 545, 1015
Beloborodov, A. M. 2002, ApJL, 566, L85
Bogdanov, S. 2013, ApJ, 762, 96
Bogdanov, S., & Grindlay, J. E. 2009, ApJ, 703, 1557
Bogdanov, S., Grindlay, J. E., Heinke, C. O., et al. 2006, ApJ, 646, 1104
Bogdanov, S., Grindlay, J. E., & Rybicki, G. B. 2008, ApJ, 689, 407
Bogdanov, S., Lamb, F. K., Mahmoodifar, S., et al. 2019, ApJL, L26
Bogdanov, S., van den Berg, M., Servillat, M., et al. 2011, ApJ, 730, 81
Braje, T. M., Romani, R. W., & Rauch, K. P. 2000, ApJ, 531, 447
Cadeau, C., Morsink, S. M., Leahy, D., & Campbell, S. S. 2007, ApJ, 654, 458
Campana, R., Orlandini, M., Del Monte, E., Feroci, M., & Frontera, F. 2014, ExA, 37, 599
Chang, P., Morsink, S., Bildsten, L., & Wasserman, I. 2006, ApJL, 636, L117
Cottam, J., Paerels, F., & Mendez, M. 2002, Natur, 420, 51
Del Pozzo, W., Li, T. G. F., Agathos, M., Van Den Broeck, C., & Vitale, S. 2013, PhRvL, 111, 071101
Durant, M., Kargaltsev, O., Pavlov, G. G., et al. 2012, ApJ, 746, 6
Faber, J. A., & Rasio, F. A. 2012, LRR, 15, 8
Fernández, R., & Metzger, B. D. 2016, ARNPS, 66, 23
Folkner, W. M., Williams, J. G., & Boggs, D. H. 2009, IPNPR, 178, 1
Forestell, L. M., Heinke, C. O., Cohn, H. N., et al. 2014, MNRAS, 441, 757
Gendreau, K. C., Arzoumanian, Z., Adkins, P. W., et al. 2016, Proc. SPIE, 9905, 99051H
Gonzalez-Caniulef, D., Guillot, S., & Reisenegger, A. 2019, MNRAS, in press (arXiv:1904.12114)
Greif, S. K., Raaijmakers, G., Hebeler, K., Schwenk, A., & Watts, A. L. 2019, MNRAS, 485, 5363
Guillot, S., Kaspi, V. M., Archibald, R. F., et al. 2016, MNRAS, 463, 2612
Guillot, S., Kerr, M., Ray, P. S., et al. 2019, ApJL, L27
Guillot, S., Servillat, M., Webb, N. A., & Rutledge, R. E. 2013, ApJ, 772, 7
Halpern, J. P., & Marshall, H. L. 1996, ApJ, 464, 760
Harding, A. K., & Muslimov, A. G. 2002, ApJ, 568, 862
Hartman, J. M., Patruno, A., Chakrabarty, D., et al. 2008, ApJ, 675, 1468
Hebeler, K., Lattimer, J. M., Pethick, C. J., & Schwenk, A. 2013, ApJ, 773, 11
Heinke, C. O. 2013, JPhCS, 432, 012001
Heinke, C. O., Cohn, H. N., Lugger, P. M., et al. 2014, MNRAS, 444, 443
Heinke, C. O., Rybicki, G. B., Narayan, R., & Grindlay, J. E. 2006, ApJ, 644, 1090
Hobbs, G. B., Edwards, R. T., & Manchester, R. N. 2006, MNRAS, 369, 655
Hui, C. Y., & Becker, W. 2006, A&A, 448, L13
Jahoda, K., Markwardt, C. B., Radeva, Y., et al. 2006, ApJS, 163, 401
Janka, H.-T., Melson, T., & Summa, A. 2016, ARNPS, 66, 341
Johnston, S., Lorimer, D. R., Harrison, P. A., et al. 1993, Natur, 361, 613
Kumar, P., & Zhang, B. 2015, PhR, 561, 1
Kuntz, K. D. 2019, A&ARv, 27, 1
Lackey, B. D., Kyutoku, K., Shibata, M., Brady, P. R., & Friedman, J. L. 2014, PhRvD, 89, 043009
Lattimer, J. M., & Prakash, M. 2001, ApJ, 550, 426
Lattimer, J. M., & Prakash, M. 2005, PhRvL, 94, 111101
Leahy, D. A., Morsink, S. M., & Chou, Y. 2011, ApJ, 742, 17
Lin, J., Özel, F., Chakrabarty, D., & Psaltis, D. 2010, ApJ, 723, 1053

Lincoln, J. V. 1967, in Physics of Geomagnetic Phenomena, ed. S. Matsushita & W. H. Campbell (New York: Academic), 67
Lo, K. H., Miller, M. C., Bhattacharyya, S., & Lamb, F. K. 2013, ApJ, 776, 19
Lockhart, W., Gralla, S. E., Özel, F., & Psaltis, D. 2019, MNRAS, 490, 1774
Lommen, A. N., Zepka, A., Backer, D. C., et al. 2000, ApJ, 545, 1007
Lynch, R. S., Swiggum, J. K., Kondratiev, V. I., et al. 2018, ApJ, 859, 93
Miller, M. C. 2013, arXiv:1312.0029
Miller, M. C., Chirenti, C., & Lamb, F. K. 2019a, ApJ, in press (arXiv:1904.08907)
Miller, M. C., & Lamb, F. K. 1998, ApJL, 499, L37
Miller, M. C., & Lamb, F. K. 2015, ApJ, 808, 31
Miller, M. C., & Lamb, F. K. 2016, EPJA, 52, 63
Miller, M. C., Lamb, F. K., Dittman, A. J., et al. 2019b, ApJL, 887, L24
Morsink, S. M., Leahy, D. A., Cadeau, C., & Braga, J. 2007, ApJ, 663, 1244
Muno, M. P., Özel, F., & Chakrabarty, D. 2002, ApJ, 581, 550
Nasa High Energy Astrophysics Science Archive Research Center (Heasarc) 2014, HEAsoft: Unified Release of FTOOLS and XANADU, Astrophysics Source Code Library, ascl:1408.004
Nättilä, J., Miller, M. C., Steiner, A. W., et al. 2017, A&A, 608, A31
Oertel, M., Hempel, M., Klähn, T., & Typel, S. 2017, RvMP, 89, 015007
Özel, F. 2013, RPPh, 76, 016901
Özel, F., & Freire, P. 2016, ARA&A, 54, 401
Özel, F., & Psaltis, D. 2009, PhRvD, 80, 103003
Özel, F., Psaltis, D., Güver, T., et al. 2016, ApJ, 820, 28
Page, D. 1995, ApJ, 442, 273
Patruno, A., & Watts, A. L. 2012, arXiv:1206.2727
Pavlov, G. G., & Zavlin, V. E. 1997, ApJL, 490, L91
Pechenick, K. R., Ftaclas, C., & Cohen, J. M. 1983, ApJ, 274, 846
Potekhin, A. Y. 2014, PhyU, 57, 735
Poutanen, J., & Beloborodov, A. M. 2006, MNRAS, 373, 836
Poutanen, J., & Gierliński, M. 2003, MNRAS, 343, 1301
Prigozhin, G., Gendreau, K., Doty, J. P., et al. 2016, Proc. SPIE, 9905, 99051I
Psaltis, D., & Özel, F. 2014, ApJ, 792, 87
Psaltis, D., Özel, F., & Chakrabarty, D. 2014, ApJ, 787, 136
Raaijmakers, G., Riley, T. E., Watts, A. L., et al. 2019, ApJL, 887, L22
Radhakrishnan, V., & Srinivasan, G. 1982, CSci, 51, 1096
Rangelov, B., Pavlov, G. G., Kargaltsev, O., et al. 2017, ApJ, 835, 264
Ransom, S. M., Ray, P. S., Camilo, F., et al. 2011, ApJL, 727, L16
Rauch, T., Suleimanov, V., & Werner, K. 2008, A&A, 490, 1127
Ray, P. S., Guillot, S., Ransom, S. M., et al. 2019, ApJL, 878, L22
Read, J. S., Baiotti, L., Creighton, J. D. E., et al. 2013, PhRvD, 88, 044042
Read, J. S., Lackey, B. D., Owen, B. J., & Friedman, J. L. 2009, PhRvD, 79, 124032
Reardon, D. J., Hobbs, G., Coles, W., et al. 2016, MNRAS, 455, 1751
Riley, T. E., Watts, A. L., Bogdanov, S., et al. 2019, ApJL, 887, L21
Romani, R. W., Slane, P., & Green, A. W. 2017, ApJ, 851, 61
Rosen, S. R., Webb, N. A., Watson, M. G., et al. 2016, A&A, 590, A1
Rosswog, S. 2015, IJMPD, 24, 1530012
Shibata, M. 2016, NuPhA, 956, 225
Shibata, M., & Taniguchi, K. 2011, LRR, 14, 6
Steiner, A. W., Heinke, C. O., Bogdanov, S., et al. 2018, MNRAS, 476, 421
Steiner, A. W., Lattimer, J. M., & Brown, E. F. 2010, ApJ, 722, 33
Strohmayer, T. E. 1992, ApJ, 388, 138
Verner, D. A., Ferland, G. J., Korista, K. T., & Yakovlev, D. G. 1996, ApJ, 465, 487
Watts, A. L. 2012, ARA&A, 50, 609
Weinberg, N., Miller, M. C., & Lamb, D. Q. 2001, ApJ, 546, 1098
Wilms, J., Allen, A., & McCray, R. 2000, ApJ, 542, 914
Yao, J. M., Manchester, R. N., & Wang, N. 2017, ApJ, 835, 29
Zavlin, V. E. 2006, ApJ, 638, 951
Zavlin, V. E., & Pavlov, G. G. 1998, A&A, 329, 583
Zavlin, V. E., Pavlov, G. G., & Shibanov, Y. A. 1996, A&A, 315, 141